Probing a heavy dark Z boson at multi-TeV muon colliders: Leveraging the optimized recoil mass technique

Kingman Cheung,[1,2,3,*] Jinheung Kim,[4,†] Soojin Lee,[1,‡] Prasenjit Sanyal,[1,5,§] and Jeonghyeon Song[1,∥]

[1]Department of Physics, Konkuk University, Seoul 05029, Republic of Korea
[2]Department of Physics, National Tsing Hwa University, Hsinchu 300, Taiwan
[3]Center for Theory and Computation, National Tsing Hua University, Hsinchu 300, Taiwan
[4]School of Physics, Korea Institute for Advanced Study, Seoul 02455, Republic of Korea
[5]Center for Quantum Spacetime, Sogang University, 35 Baekbeom-ro, Seoul 121-742, Republic of Korea

(Received 10 January 2025; accepted 30 September 2025; published 10 November 2025)

We investigate the discovery potential of multi-TeV muon colliders for a heavy dark Z boson (Z_{D}) with a mass above 1 TeV, via the associated production process $\mu^+\mu^- \to Z_{\mathrm{D}}\gamma$. This process enables precise reconstruction of $M_{Z_{\mathrm{D}}}$ through the photon recoil mass (m_{recoil}). Focusing on the $Z_{\mathrm{D}} \to jjX$ and $Z_{\mathrm{D}} \to e^+e^-$ decay modes, we present strategies to achieve high sensitivity to the kinetic mixing parameter ε at 3, 6, and 10 TeV muon colliders with integrated luminosities of 1, 4, and 10 ab^{-1}, respectively, assuming that Z_{D} decays exclusively into Standard Model particles. We apply mass-dependent cuts on m_{recoil} and m_{ee} to account for the energy-dependent detector response. For heavier $M_{Z_{\mathrm{D}}}$, the associated photon becomes less energetic, leading to better photon energy resolution and enabling more stringent m_{recoil} cuts. Conversely, for lighter $M_{Z_{\mathrm{D}}}$, the lower-energy electron pair from $Z_{\mathrm{D}} \to e^+e^-$ allows tighter invariant mass (m_{ee}) cuts. By combining these complementary m_{recoil}- and m_{ee}-based selections across both the jjX and e^+e^- channels, we achieve sensitivity to ε down to $\mathcal{O}(10^{-3})$ as $M_{Z_{\mathrm{D}}}$ approaches $\sqrt{s}$, substantially surpassing the projected reach of a 100 TeV proton-proton collider. Even if Z_{D} decays into dark-sector particles, the recoil mass method remains effective, highlighting muon colliders as powerful facilities for exploring heavy dark sectors.

DOI: 10.1103/pm8d-ts6c

I. INTRODUCTION

Our Universe is described by the Standard Model (SM) of particle physics, which has been thoroughly tested and confirmed, culminating in the landmark discovery of the Higgs boson at the Large Hadron Collider (LHC) in 2012 [1,2]. Despite this achievement, major unresolved puzzles persist: the fundamental properties of dark matter and dark energy, the origin of neutrino masses, and the matter-antimatter asymmetry. These profound questions strongly suggest that the SM is incomplete, motivating the search for new particles and interactions predicted by beyond the Standard Model (BSM) theories. High-energy collider experiments offer a controlled and precisely instrumented environment for these investigations. Yet, despite extensive efforts, the LHC has not uncovered direct evidence of BSM particles, underscoring the complexity of such probes.

In light of this challenge, a new paradigm emerged: the dark sector. Instead of assuming that new particles carry SM gauge charges, this scenario envisions them residing in a separate sector that interacts with our visible world only through a portal. One of the most compelling and minimal portals is realized by a dark $U(1)$ gauge boson Z_{D}, which couples to the SM through kinetic mixing with a SM Abelian gauge boson [3–7]. This approach minimally extends the gauge principle and introduces a dimension-four mixing operator. If the dark sector particles are heavier than Z_{D}, ensuring Z_{D} decays exclusively into SM particles, then the Z_{D} phenomenology depends only on its mass $M_{Z_{\mathrm{D}}}$ and the kinetic mixing parameter ε.

Extensive experimental efforts have tightly constrained the lighter Z_{D} mass range through a combination of fixed-target, beam-dump, and collider experiments, as well as astrophysical observations. For 1 MeV $\lesssim M_{Z_{\mathrm{D}}} \lesssim$ 30 MeV, a wide range of $\varepsilon > \mathcal{O}(10^{-9})$ is excluded at the 2σ level by supernova bounds [8], beam-dump experiments such as

*Contact author: cheung@phys.nthu.edu.tw
†Contact author: jhkim1216@kias.re.kr
‡Contact author: soojinlee957@gmail.com
§Contact author: prasenjit.sanyal01@gmail.com
∥Contact author: jhsong@konkuk.ac.kr

E774 [9], CHARM [10], ν-Cal [11,12], and E141 [13], as well as by NA64(e) [14], NA48/2 [15], and $(g-2)_e$ measurements [16].

For $30\ \text{MeV} \lesssim M_{Z_D} \lesssim \mathcal{O}(1)$ GeV, current collider experiments including NA48/2 [17], A1 [18], *BABAR* [19], KLOE [20,21], and LHCb [22] have excluded the values of ε above approximately $\mathcal{O}(10^{-4})$. These bounds will be further improved by upcoming experiments such as Belle II [23] and the upgraded LHCb [24,25]. Numerous beam-dump experiments—including E137 [26–28], CHARM [29], and NuCal [11,12]—also provide strong constraints in the range $\varepsilon \sim \mathcal{O}(10^{-4})$–$\mathcal{O}(10^{-7})$. These constraints will be extended by future facilities [30], including NA62 [31], NA64 [14], FASER/FASER2 [32,33], SeaQuest [34], HPS [35], AWAKE [36], and MESA [37,38].

For $M_{Z_D} \gtrsim \mathcal{O}(10)$ GeV, the strongest current limits come from running hadron colliders, notably CMS [39], which constrains $M_{Z_D} \lesssim 200$ GeV. The High-Luminosity LHC (HL-LHC) is expected to extend the reach to $M_{Z_D} \sim 1$ TeV. Looking ahead, future e^+e^- facilities such as FCC-ee [40], ILC [41,42], and CEPC [43] offer significant projected sensitivity for $M_{Z_D} \sim \mathcal{O}(100)$ GeV. In particular, the recoil-mass technique against an ISR photon at future e^+e^- colliders shows promising reach [42,44]. Future hadron colliders will also contribute substantially in this mass window; for example, FCC-hh at $\sqrt{s} = 100$ TeV with $\mathcal{L}_{\text{tot}} = 3\ \text{ab}^{-1}$ is projected to probe indirect effects via electroweak precision observables [45], reaching sensitivities down to $\varepsilon \sim \mathcal{O}(10^{-3})$ for $M_{Z_D} \in [10, 80]$ GeV.

However, for a heavy Z_D with a mass above 1 TeV, existing constraints are much weaker. Most previous studies have focused on proton–proton (pp) colliders through the Drell-Yan process. At the HL-LHC, with an integrated luminosity of $\mathcal{L}_{\text{tot}} = 3\ \text{ab}^{-1}$, the projected sensitivity reaches $\varepsilon \sim 10^{-2}$ and $\varepsilon \sim 0.1$ for $M_{Z_D} = 1$ TeV and 2.4 TeV, respectively. A future 100 TeV pp collider with 3 ab^{-1} could improve these limits to $\varepsilon \sim 4 \times 10^{-3}$ and $\varepsilon \sim 3 \times 10^{-2}$ for the same mass benchmarks [45]. Even at the canonical luminosity of 30 ab^{-1}, the gain remains modest. In the background-dominated regime, the sensitivity limit scales as $\varepsilon \propto \mathcal{L}_{\text{tot}}^{-1/4}$, since the signal cross section itself grows as $\propto \varepsilon^2$. Consequently, increasing the luminosity from 3 ab^{-1} to 30 ab^{-1} improves the reach only to about $0.56\varepsilon_{3\ \text{ab}^{-1}}$. Furthermore, as M_{Z_D} increases, the production cross section falls sharply due to the rapid decline of partonic luminosities at large $\sqrt{\hat{s}}$, which strongly suppresses the Drell–Yan process [46]: see Fig. 8. Given that a 100 TeV pp collider also remains a distant prospect, it is therefore imperative to explore alternative approaches for probing such heavy Z_D masses.

A multi-TeV muon collider (MuC) [47–49] offers a promising solution. Capable of achieving multi-TeV center-of-mass (c.m.) energies in a relatively clean environment, the MuC can fully exploit its collision energy for BSM searches [50–54]. Previous studies have shown that MuCs excel at probing heavy new particles, surpassing hadron colliders in their kinematic reach [55–58]. Recent progress in muon beam cooling [59,60] and in managing beam-induced backgrounds (BIBs) [61,62] has made the MuC increasingly realistic. Although indirect effects of a dark Z at a MuC have been investigated for moderate masses below about 1.5 TeV [63], direct search strategies for a heavy Z_D at multi-TeV MuCs remain largely unexplored.

One of the most powerful techniques to enhance the discovery potential of a MuC for the heavy Z_D is the recoil mass (m_{recoil}) method, which takes full advantage of the known initial-state kinematics in lepton collisions [64–75]. In particular, the associated production channel $\mu^+\mu^- \to Z_D\gamma$ is promising: the known c.m. energy and the measured photon energy E_γ determine M_{Z_D} via $m^2_{\text{recoil}} = s - 2\sqrt{s}E_\gamma$, without assumptions about how Z_D decays. This recoil mass technique cannot be employed at hadron colliders due to unknown initial parton energies. Furthermore, the $Z_D \to e^+e^-$ decay mode provides a complementary mass reconstruction method through the e^+e^- invariant mass m_{ee}. In contrast, the $Z_D \to \mu^+\mu^-$ decay mode suffers from larger backgrounds than the $Z_D \to e^+e^-$ mode, due to t-channel and vector boson fusion (VBF) processes at the MuC. Therefore, we do not consider the $Z_D \to \mu^+\mu^-$ decay mode in this analysis.

While the recoil mass method is well established, many analyses typically employ universal, mass-independent cuts on both m_{recoil} and m_{ee} without accounting for energy resolution effects at the detector level. Building on approaches used in previous studies [19,42,76–83], we employ M_{Z_D}- and $\sqrt{s}$-dependent mass cuts optimized for MuC environments. Since a heavier Z_D is produced with a softer accompanying photon—and photon energy resolution generally improves at lower energies [64]—we impose tighter m_{recoil} selections for larger M_{Z_D}, using the resolution parameters implemented in the latest Delphes [84] muon-collider detector card. This strategy significantly enhances the ε sensitivity in the heavier mass regime. Meanwhile, for the $Z_D \to e^+e^-$ channel, a lighter Z_D produces a lower-energy electron pair, enabling tighter m_{ee} cuts. Therefore, the interplay of m_{recoil}- and m_{ee}-based selections ensures robust coverage across a broad M_{Z_D} range. Combined with the increasing cross section of $\mu^+\mu^- \to Z_D\gamma$ as M_{Z_D} approaches $\sqrt{s}$, our method opens a powerful new channel for probing heavy Z_D, which represents our primary contribution.

The organization of this paper is as follows. In Sec. II, we briefly review the theory of kinetically mixed $U(1)_D$. Drawing on the characteristic features of the heavy dark Z, we identify the golden channels to probe Z_D at a multi-TeV MuC. Section III discusses mass reconstruction techniques in detail, including the introduction of M_{Z_D}- and $\sqrt{s}$-dependent resolutions for m_{recoil} and m_{ee}. In Sec. IV, we present our event selection, applying mass-dependent cuts for both m_{recoil} and m_{ee} and demonstrating the resulting improvements in ε sensitivity. We then offer sensitivity projections for various MuC energies, highlighting the complementarity of the jjX and e^+e^- decay modes across different M_{Z_D} regimes, and compare our results with other future pp colliders. Finally, we conclude in Sec. V, summarizing our findings and discussing the implications for future dark sector searches.

II. THEORY OF HEAVY DARK Z AND IDENTIFICATION OF GOLDEN DISCOVERY CHANNELS AT MUON COLLIDERS

In this section, we briefly review the theoretical framework of the dark Z boson Z_D, which emerges from kinetic mixing with the SM hypercharge gauge field $\tilde{B}_\mu$. The relevant Lagrangian terms are given by [6]

$$\mathscr{L} \supset -\frac{1}{4}\tilde{B}_{\mu\nu}\tilde{B}^{\mu\nu} - \frac{1}{4}\tilde{Z}_{D\mu\nu}\tilde{Z}_D^{\mu\nu} - \frac{1}{2}\frac{\varepsilon}{c_W}\tilde{Z}_{D\mu\nu}\tilde{B}^{\mu\nu} + \frac{1}{2}M_{D,0}^2\tilde{Z}_D^\mu\tilde{Z}_{D\mu}, \tag{1}$$

where $\tilde{B}^{\mu\nu} = \partial^\mu\tilde{B}^\nu - \partial^\nu\tilde{B}^\mu$ and $\tilde{Z}_D^{\mu\nu} = \partial^\mu\tilde{Z}_D^\nu - \partial^\nu\tilde{Z}_D^\mu$. Here, $c_W = \cos\theta_W$ denotes the cosine of the Weinberg angle θ_W. For convenience, we introduce the simplified notation $s_x = \sin x$, $c_x = \cos x$, and $t_x = \tan x$. To probe parameter regions that remain relatively unexplored by current and future collider experiments, we focus on a heavy dark Z scenario with small kinetic mixing

$$M_{Z_D} \in [1, 10]\ \text{TeV}, \qquad \varepsilon < 10^{-1}. \tag{2}$$

The mass term in Eq. (1) can originate from a Stueckelberg mechanism [85] or a dark Higgs mechanism 6,45]], but its underlying source does not critically impact our main conclusions. For heavy masses satisfying Eq. (2), we introduce a small mass ratio parameter

$$\delta_m = \frac{m_{Z,0}}{M_{D,0}} \ll 1, \tag{3}$$

where $m_{Z,0} = gv/(2c_W)$ with $v \approx 246$ GeV.

The field redefinition of

$$\begin{pmatrix} Z_{D,0}^\mu \\ B^\mu \end{pmatrix} = \begin{pmatrix} \sqrt{1-\frac{\varepsilon^2}{c_W^2}} & 0 \\ \frac{\varepsilon}{c_W} & 1 \end{pmatrix} \begin{pmatrix} \tilde{Z}_D^\mu \\ \tilde{B}^\mu \end{pmatrix} \tag{4}$$

diagonalizes the kinetic terms of the gauge bosons. After the electroweak symmetry breaking, the mass-squared matrix in the basis of $(A^\mu, Z_0^\mu, Z_{D,0}^\mu)$ becomes

$$\mathcal{M}_V^2 = M_{D,0}^2 \begin{pmatrix} 0 & 0 & 0 \\ 0 & \delta_m^2 & t_W\delta_m^2\varepsilon \\ 0 & t_W\delta_m^2\varepsilon & 1 \end{pmatrix} + \mathcal{O}(\delta_m^2\varepsilon^2), \tag{5}$$

which clearly shows a massless photon.

The physical Z and Z_D mass eigenstates are obtained through the mixing matrix

$$\begin{pmatrix} Z \\ Z_D \end{pmatrix} = \begin{pmatrix} c_\alpha & s_\alpha \\ -s_\alpha & c_\alpha \end{pmatrix} \begin{pmatrix} Z_0 \\ Z_{D,0} \end{pmatrix}, \tag{6}$$

where the mixing angle α is given by

$$\alpha = -t_W\delta_m^2\varepsilon + \mathcal{O}(\delta_m^4\varepsilon). \tag{7}$$

The masses of the physical Z and Z_D are

$$m_Z = m_{Z,0}\left[1 - \frac{1}{2}t_W^2\delta_m^2\varepsilon^2 + \mathcal{O}(\delta_m^4\varepsilon^2)\right],$$
$$M_{Z_D} = M_{D,0}\left[1 + \frac{1}{2}t_W^2\delta_m^2\varepsilon^2 + \mathcal{O}(\delta_m^4\varepsilon^2)\right]. \tag{8}$$

Thus, Z and Z_D are canonically normalized and have well-defined masses.

The interaction Lagrangian for Z and Z_D couplings to SM fermions is parametrized by

$$-\mathscr{L}_{\text{int}}^f = \frac{g}{c_W}\hat{g}_Z^f Z^\mu \bar{f}\gamma_\mu f + \varepsilon\frac{g}{c_W}\hat{g}_{Z_D}^f Z_D^\mu \bar{f}\gamma_\mu f. \tag{9}$$

The normalized couplings are given by

$$\hat{g}_Z^f = T_{3f} - Q_f s_W^2 - (T_{3f} - Q_f)t_W^2\delta_m^2\varepsilon^2 + \mathcal{O}(\delta_m^4\varepsilon^2),$$
$$\hat{g}_{Z_D}^f = (T_{3f} - Q_f)t_W + \mathcal{O}(\delta_m^2), \tag{10}$$

where T_{3f} and Q_f are the third component of weak isospin and the electric charge for the fermion f, respectively. Through the Z and Z_D mixing in Eq. (6), the dark Z also couples to W^+W^- and ZH, where H is the 125 GeV Higgs boson.

With these interaction vertices established, we now turn to the decay channels of Z_D. To facilitate a direct comparison with existing LHC sensitivity limits, we do not consider Z_D decays into BSM states such as dark matter [75,86]. Instead, we focus solely on decays into SM particles, following the same setup employed in the conventional LHC searches [19,22,87–98]. This approach allows us to clearly demonstrate the improved ε sensitivity at a multi-TeV MuC.

For $M_{Z_D} > 1$ TeV, the dominant Z_D decays are into SM fermion pairs, including top quarks. However, the relative importance of a specific decay channel differs significantly from that of the SM Z boson. For instance, the ratios

$$\frac{\hat{g}_{Z_\mathrm{D}}^{\nu_L}}{\hat{g}_{Z}^{\nu_L}} = t_\mathrm{W} \approx 0.548,$$
$$\frac{\hat{g}_{Z_\mathrm{D}}^{e_R}}{\hat{g}_{Z}^{e_R}} = \frac{1}{s_\mathrm{W} c_\mathrm{W}} \approx 2.37, \qquad \frac{\hat{g}_{Z_\mathrm{D}}^{e_L}}{\hat{g}_{Z}^{e_L}} = \frac{t_\mathrm{W}}{2s_\mathrm{W}^2 - 1} \approx -1.02, \qquad (11)$$

show that neutrino modes are relatively suppressed, whereas the decay into an electron-positron pair is enhanced.

The branching ratios remain nearly constant for $M_{Z_\mathrm{D}} \geq 1$ TeV

$$\sum_q \mathrm{Br}(Z_\mathrm{D} \to q\bar{q}) \approx 0.40, \quad \mathrm{Br}(Z_\mathrm{D} \to t\bar{t}) \approx 0.13,$$
$$\sum_\ell \mathrm{Br}(Z_\mathrm{D} \to \nu_\ell \bar{\nu}_\ell) \approx 0.074, \quad \sum_\ell \mathrm{Br}(Z_\mathrm{D} \to \ell^+\ell^-) \approx 0.36,$$
$$\mathrm{Br}(Z_\mathrm{D} \to W^+W^-) \approx 0.019, \quad \mathrm{Br}(Z_\mathrm{D} \to ZH) \approx 0.013, \qquad (12)$$

where $q = u$, d, c, s, b, and $\ell = e$, μ, τ. At masses $M_{Z_\mathrm{D}} > 1$ TeV, the branching ratios into different lepton flavors become equal. We note that the suppression of the neutrino decay mode, combined with the enhancement of the charged lepton decay channel, distinguishes the heavy Z_D from the SM Z boson.

In light of these patterns, we focus on two key decay modes at the MuC

$$Z_\mathrm{D} \to jj + X, \qquad Z_\mathrm{D} \to e^+e^-. \qquad (13)$$

The inclusive dijet mode combines multiple hadronic final states ($q\bar{q}$, $\tau^+\tau^-$, $t\bar{t}$, and W^+W^-), maximizing the signal event yield and enhancing sensitivity. For our analysis of the leptonic decay, we focus on the e^+e^- final state rather than the $\mu^+\mu^-$ channel. The $\mu^+\mu^-$ channel faces significant backgrounds from t-channel and VBF processes that produce muons in the final state. At a multi-TeV muon collider, background processes involving diagrams with direct connections to the initial- and final-state muon lines have greatly enhanced cross sections. The e^+e^- final state, in contrast, does not suffer from this t-channel enhancement. To avoid these large backgrounds, we do not consider the $Z_\mathrm{D} \to \mu^+\mu^-$ channel in this study.

We now examine the production of a heavy dark Z boson at a multi-TeV MuC. Direct production via an s-channel resonance, $\mu^+\mu^- \to Z_\mathrm{D}$, is inefficient as it requires the c.m. energy to be tuned to the boson's mass, $\sqrt{s} \approx M_{Z_\mathrm{D}}$. Although initial-state radiation (ISR) can broaden the accessible mass range, this effect is less pronounced for muons than for electrons, limiting this approach at a MuC. Instead, associated production with SM particles through $2 \to 2$ or $2 \to 3$ processes is more promising. This strategy offers two key advantages. First, it enables the exploration of a wide mass range with $M_{Z_\mathrm{D}} < \sqrt{s}$. Second, the additional hard SM particles in the final state provide a powerful tool for suppressing the beam-induced background (BIB).

The BIB is a distinctive challenge at MuCs, arising from the decays of muons in the beamline. The decay products—primarily high-energy electrons and positrons—and their subsequent synchrotron radiation photons interact with machine elements, producing secondary particles. To protect the detector, tungsten nozzles are placed around the interaction point, which absorb most of the high-energy decay products but in turn become a source of lower-energy background particles that enter the detector volume [99]. These cascades produce large fluxes of secondary photons, neutrons, electrons/positrons ($e^\pm$), charged hadrons, and Bethe-Heitler muons [99,100]. The resulting background exhibits high multiplicity and a broad timing distribution, with many particles arriving out of time with respect to the bunch crossing, which allows for significant suppression using precision timing detectors [99].

Owing to the shielding nozzles (and the resulting timing profile), most BIB particles that reach the detector are both relatively soft and largely out of time. The flux is dominated by photons and electrons with mean momenta of only a few MeV; charged and neutral hadrons have mean momenta of about half a GeV, while only the comparatively rare Bethe-Heitler muons exhibit higher mean momenta near 14 GeV [100]. Consequently, under selections that require high-p_T, in-time SM objects in the central detector, BIB does not constitute a significant *physics background*; its primary impact is on detector occupancy rather than irreducible contamination.

Motivated by these considerations, we examine three primary production channels

$$\mu^+\mu^- \to Z_\mathrm{D}\gamma, \qquad (14)$$

$$\mu^+\mu^- \to Z_\mathrm{D}\nu\bar{\nu}, \qquad (15)$$

$$\mu^+\mu^- \to Z_\mathrm{D}\mu^+\mu^-, \qquad (16)$$

where ν includes all three flavors. Note that the $\mu^+\mu^- \to Z_\mathrm{D}Z^{(*)}$ production channel is also possible and is partially included in the processes of Eqs. (15) and (16). We do not consider $Z^{(*)} \to jj$ and $Z^{(*)} \to e^+e^-$ to avoid combinatorial ambiguities arising from identical final states produced by both Z_D and Z decays. Thus, we focus exclusively on the three production channels listed above.

Figure 1 shows the parton-level cross sections (normalized by ε^2) as a function of M_{Z_D} at $\sqrt{s} = 3$ TeV (left) and $\sqrt{s} = 10$ TeV (right), obtained using MadGraph5-aMC@NLO [101] version 3.5.1. For the $Z_\mathrm{D}\gamma$ and $Z_\mathrm{D}\mu^+\mu^-$ channels, we require $p_T^{\gamma,\mu} \geq 10$ GeV and $|\eta_{\gamma,\mu}| \leq 2.5$, while for the $Z_\mathrm{D}\nu\bar{\nu}$ channel we impose $E_T^\mathrm{miss} \geq 20$ GeV.

At both 3 TeV and 10 TeV MuC energies, the $\mu^+\mu^- \to Z_\mathrm{D}\gamma$ channel typically yields the largest cross section,

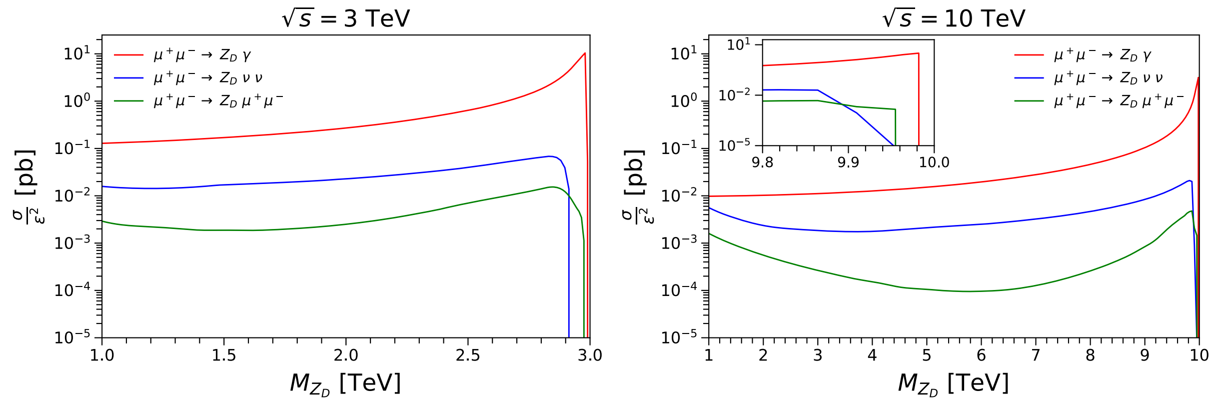

FIG. 1. Cross sections of heavy dark Z production as a function of M_{Z_D} through $\mu^+\mu^- \to Z_D\gamma$ (red), $\mu^+\mu^- \to Z_D\nu\bar{\nu}$ (blue), and $\mu^+\mu^- \to Z_D\mu^+\mu^-$ (green) at MuCs with $\sqrt{s} = 3$ TeV (left) and $\sqrt{s} = 10$ TeV (right). The cross sections are normalized by ε^2.

followed by $\mu^+\mu^- \to Z_D\nu\bar{\nu}$ and then $\mu^+\mu^- \to Z_D\mu^+\mu^-$. As M_{Z_D} approaches $\sqrt{s}$, the $Z_D\gamma$ cross section rises sharply because the photon becomes softer, effectively reducing the process to a $2 \to 1$ configuration. This behavior contrasts with Drell-Yan process at pp colliders, $pp \to Z_D$, where higher M_{Z_D} values result in significantly smaller cross sections due to the limited parton distribution functions at large momentum fractions. For instance, at a 100 TeV pp collider, $\sigma(pp \to Z_D)/\varepsilon^2 = 140, 0.5, 0.03$ pb for $M_{Z_D} = 1, 5, 10$ TeV, respectively. We note, however, that as $m_{Z'}$ nears $\sqrt{s}$ at the MuC, the requirement of a hard initial-state radiation photon (e.g., $p_T^\gamma > 10$ GeV) severely constrains the available phase space, causing the production cross section to drop precipitously.

The second largest cross sections occur for $\mu^+\mu^- \to Z_D\nu\bar{\nu}$, which benefits from three neutrino flavors and VBF contributions at high energies [102]. In contrast, $\mu^+\mu^- \to Z_D\mu^+\mu^-$ is suppressed due to the absence of a Z-Z-Z_D vertex, which is required for neutral-current VBF processes.

Combining these insights on production and decay, we identify two "golden" discovery modes for heavy Z_D at the MuC: $\mu^+\mu^- \to Z_D\gamma$ followed by $Z_D \to jj + X$ or $Z_D \to e^+e^-$. These channels provide the strongest prospects for discovering a heavy dark Z at future multi-TeV MuCs.

Finally, let us make brief comments on the subtle differences in the behavior of the production cross sections for the three proposed production channels, as M_{Z_D} approaches $\sqrt{s}$. The presented cross sections are calculated after imposing minimal kinematic cuts: for $\mu^+\mu^- \to Z_D\gamma$, $p_T^\gamma \geq 10$ GeV and $|\eta_\gamma| \leq 2.5$; for $\mu^+\mu^- \to Z_D\mu^+\mu^-$, $p_T^\mu \geq 10$ GeV and $|\eta_\mu| \leq 2.5$; and for $\mu^+\mu^- \to Z_D\nu\bar{\nu}$, $E_T^{\text{miss}} \geq 20$ GeV. These kinematic cuts restrict the available phase space differently depending on the production process.

In particular, the universal condition $E_T^{\text{miss}} \geq 20$ GeV for both the 3 TeV and 10 TeV MuCs leads to the apparent difference in the behavior of the $Z_D\nu\bar{\nu}$ cross section as M_{Z_D} approaches $\sqrt{s}$. At the 3 TeV MuC, this cut acts as a relatively stringent requirement, significantly suppressing the cross section for higher M_{Z_D} values and causing it to decline well before reaching the kinematic limit at $\sqrt{s}$. In contrast, at the 10 TeV MuC, the same 20 GeV missing-energy cut is relatively mild compared to the total collision energy, allowing the cross section to extend much closer to the kinematic threshold at $M_{Z_D} \approx \sqrt{s}$.

Nevertheless, the E_T^{miss} cut results in a consistent qualitative behavior: as M_{Z_D} approaches $\sqrt{s}$, the cross section for $\mu^+\mu^- \to Z_D\nu\bar{\nu}$ decreases more rapidly than for $\mu^+\mu^- \to Z_D\mu^+\mu^-$. This trend is readily apparent for the 3 TeV case in Fig. 1; to better illustrate this feature for the 10 TeV case where it is less clear, we include a zoomed-in panel in the right-hand plot.

III. PRECISION MEASUREMENT OF HEAVY DARK Z MASS AT MUON COLLIDERS

A. Experimental conditions of muon colliders

This subsection outlines the experimental parameters and simulation setup for our analysis. We consider three multi-TeV MuC scenarios:[1]

(i) $\sqrt{s} = 3$ TeV with $\mathcal{L}_{\text{tot}} = 1$ ab^{-1};
(ii) $\sqrt{s} = 6$ TeV with $\mathcal{L}_{\text{tot}} = 4$ ab^{-1}; and
(iii) $\sqrt{s} = 10$ TeV with $\mathcal{L}_{\text{tot}} = 10$ ab^{-1}.

[1]In a recent update, the International Muon Collider Collaboration identified $\sqrt{s} = 3$ TeV and 10 TeV as the principal staging options, and a 6 TeV machine is no longer considered a primary scenario [103]. Nonetheless, we include the 6 TeV configuration, which has been extensively explored in the literature [66,99,104–109], as it provides a valuable interpolation between the 3 and 10 TeV benchmarks. Including this intermediate point helps clarify a key trend for our analysis: as $\sqrt{s}$ increases at a fixed M_{Z_D}, the initial-state radiation photon becomes harder, which degrades the recoil-mass resolution. This effect partially offsets the gains from higher c.m. energy, and the 6 TeV results sharpen the interpretation of this scaling behavior.

The integrated-luminosity benchmarks are taken from representative parameter sets used in recent MuC design and phenomenology studies [55,104,105,110]. They reflect a comprehensive machine optimization for each energy scale.

The detector response is simulated using Delphes version 3.5.1 [84] with the `delphes_card_MuonColliderDet.tcl` configuration card. This setup provides a parametric approximation of detector performance and is a standard choice for phenomenological studies at MuCs [55,103,105]. We acknowledge that this general parametrization does not yet implement the specific details of the latest detector concepts currently under development, namely MAIA [111,112] and MUSIC [103,111]. However, as a final detector design has not yet been selected, the Delphes framework provides an effective and robust baseline for assessing physics sensitivity. The projections presented in our study are therefore concept-agnostic and can be readily reinterpreted for any specific detector architecture once its parameters are finalized.

A crucial aspect of our detector-level simulation is the energy resolution of photons, electrons, and positrons, since the analysis relies on reconstructing the $Z_{\rm D}$ mass from their measured energies. The energy resolution of a photon, ΔE_γ, at the detector is parametrized as

$$\frac{\Delta E_\gamma}{E_\gamma} = \frac{a}{\sqrt{E_\gamma}} \oplus b \oplus \frac{c}{E_\gamma}, \qquad (17)$$

where E_γ is measured in GeV and $\oplus$ denotes addition in quadrature. In the `delphes_card_MuonColliderDet.tcl`, the parameters are set to $b = 0.01$ and $c = 0$, while a varies with pseudorapidity: $a = 0.156$ for $|\eta_\gamma| \le 0.78$, $a = 0.175$ for $0.78 \le |\eta_\gamma| \le 0.83$, and $a = 0.151$ for $0.83 \le |\eta_\gamma| \le 2.5$. The energy resolution parameters for electrons and positrons in the Delphes card are set to be identical to those for photons.

Finally, we address the treatment of the BIB in our analysis. As detailed earlier, the primary impact of the soft, out-of-time BIB is on detector occupancy rather than creating an irreducible physics background for high-p_T, in-time objects. To account for the residual BIB in our fast simulation, we therefore adopt a simplified strategy based on fiducial acceptance. We restrict all reconstructed objects to the central, better-protected region of the detector (e.g., $|\eta| < 2.5$), consistent with the geometric coverage implied by the shielding-nozzle design. This approach is sufficient for the high-energy, central signatures considered in this analysis.

B. Resolution of the heavy dark Z mass

Having identified two golden channels in the previous section, we now address a key component of our analysis: the precise measurement of the heavy $Z_{\rm D}$ mass. Accurate determination of $M_{Z_{\rm D}}$ is essential for efficient background suppression, thereby forming the backbone of our analysis strategy.

A common approach to measuring $M_{Z_{\rm D}}$ is to use the resonance peak in the invariant mass of the $Z_{\rm D}$ decay products. For the $Z_{\rm D} \to e^+e^-$ channel, the invariant mass of the electron-positron pair (m_{ee}) directly provides this resonance. However, this method does not work for the inclusive dijet mode from $Z_{\rm D} \to t\bar{t}$, $Z_{\rm D} \to \tau^+\tau^-$, and $Z_{\rm D} \to W^+W^-$.

Fortunately, the $Z_{\rm D}$ production channel associated with a photon offers a powerful alternative: measuring the recoil mass of the photon, $m_{\rm recoil}$. For the process

$$\mu^-(p_1) + \mu^+(p_2) \to Z_{\rm D}(p_{Z_{\rm D}}) + \gamma(p_\gamma), \qquad (18)$$

$m_{\rm recoil}$ is defined by

$$m^2_{\rm recoil} = (p_1 + p_2 - p_\gamma)^2 = M^2_{Z_{\rm D}} = s - 2\sqrt{s}E_\gamma, \qquad (19)$$

where the last equality holds in the c.m. frame. Thus, the heavy dark Z mass is uniquely determined by $\sqrt{s}$ and the photon energy. This recoil mass technique is a well-established method for BSM searches at lepton colliders [64–75].

While some existing studies employ a fixed mass window cut—for instance, $|m_{{\rm recoil},ee} - M_{Z_{\rm D}}| < 10$ GeV—regardless of the $M_{Z_{\rm D}}$ value [66], this approach can be suboptimal. The widths of the reconstructed recoil mass ($m_{\rm recoil}$) and invariant mass (m_{ee}) distributions vary significantly with both $M_{Z_{\rm D}}$ and $\sqrt{s}$. This variation is a direct consequence of the energy-dependent detector response, as the energy resolution for photons, electrons, and positrons depends on their respective energies.

Consequently, a fixed cut is not universally optimal across the entire mass range. If the actual mass resolution for a given mass is wider than the cut, signal efficiency is unnecessarily lost. Conversely, if the resolution is narrower, the cut is too permissive and accepts excess background. In either case, the signal significance is degraded.

Figure 2 illustrates this point by presenting the normalized distributions of $m_{\rm recoil}$ (blue) and m_{ee} (orange) for the process $\mu^+\mu^- \to Z_{\rm D}(\to e^+e^-)\gamma$ through fast detector-level simulations. The results are shown for $\sqrt{s} = 3$ TeV (upper panels) and $\sqrt{s} = 10$ TeV (lower panels). For this simulation, parton-level events were generated using MadGraph5-aMC@NLO [101] and subsequently processed with Pythia 8.307 [113] for parton showering and hadronization. The final detector response was then simulated with Delphes.

We first observe that the $m_{\rm recoil}$ distribution is much broader for lighter $M_{Z_{\rm D}}$ (corresponding to higher-energy photons) and becomes sharper for heavier $M_{Z_{\rm D}}$ (corresponding to lower-energy photons). For example, at a

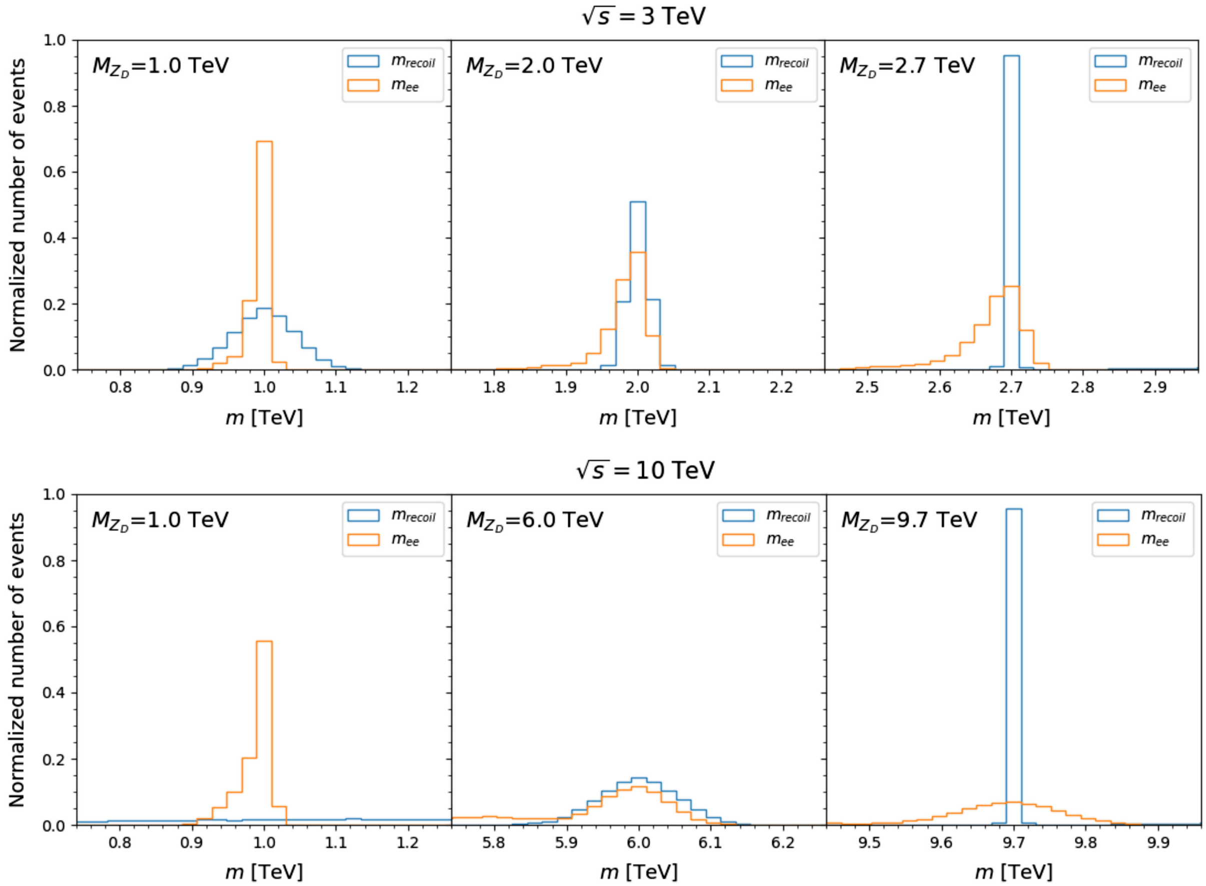

FIG. 2. Normalized distributions of the recoil mass m_{recoil} (blue) and the e^+e^- invariant mass m_{ee} (orange) for $\mu^+\mu^- \to Z_D(\to e^+e^-)\gamma$ at $\sqrt{s} = 3$ TeV (upper panels) and $\sqrt{s} = 10$ TeV (lower panels) MuC.

10 TeV MuC, we find $\Delta E_\gamma \approx 50$ GeV for $M_{Z_D} = 1$ TeV, compared to only $\Delta E_\gamma \approx 2$ GeV for $M_{Z_D} = 9.8$ TeV.

Obviously, the m_{ee} distribution exhibits the opposite trend, becoming broader for heavier M_{Z_D}, as shown in Fig. 2. Another distinctive feature is its increasingly asymmetric shape with a pronounced tail toward lower values, as M_{Z_D} increases. To illustrate this asymmetry in detail, Fig. 3 shows the m_{ee} distribution for $M_{Z_D} = 6$ TeV at a 10 TeV MuC. Several factors contribute to this behavior: the energy and momentum resolution at the detector degrades for more energetic electrons and positrons; bremsstrahlung losses become more significant at higher energies, shifting the measured energies downward; and final-state radiation (FSR) is particularly pronounced for electrons and positrons due to their low mass. Collectively, these effects lead to a broader distribution with a shift toward lower reconstructed masses as M_{Z_D} increases.

These contrasting behaviors of the m_{recoil} and m_{ee} distributions emphasize the importance of adopting different mass window cuts for each observable, tailored to M_{Z_D}. For the selection on the m_{recoil} and m_{ee} mass windows, parametrized by

$$|m_{\mathrm{recoil}} - M_{Z_D}| < 2\Delta m_{\mathrm{recoil}}, \qquad |m_{ee} - M_{Z_D}| < 2\Delta m_{ee}, \tag{20}$$

we adjust $\Delta m_{\mathrm{recoil}}$ and Δm_{ee} as functions of M_{Z_D} and $\sqrt{s}$ to improve the ε sensitivity across the full mass range.

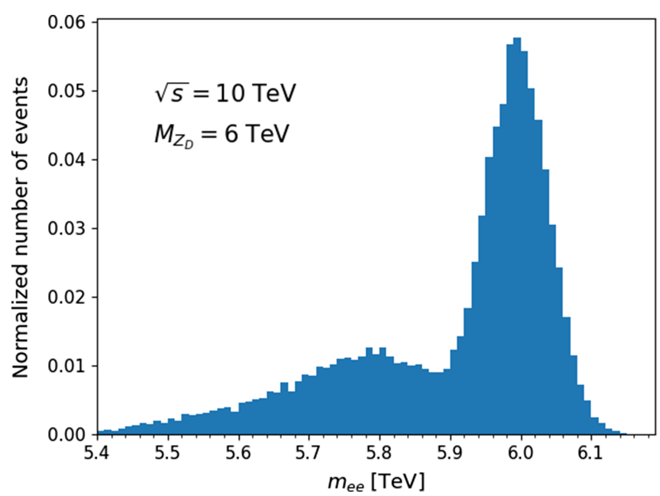

FIG. 3. Normalized distributions of the m_{ee} invariant mass for $\mu^+\mu^- \to Z_D\gamma$ with $M_{Z_D} = 6$ TeV at the 10 TeV MuC.

To estimate the optimal mass resolutions, $\Delta m_{\mathrm{recoil}}$ and Δm_{ee}, we performed fast detector-level simulations at multiple M_{Z_D} benchmark points for MuC energies of 3, 6, and 10 TeV [55,105,114,115], following the same procedure detailed in the discussion of Fig. 2. For each combination of M_{Z_D} and $\sqrt{s}$, we define the resolution as the standard deviation of a Gaussian function fitted to the corresponding m_{recoil} or m_{ee} distribution.

However, this simple Gaussian fit is complicated by the m_{ee} distribution's long, asymmetric tail toward lower mass values, which artificially inflates the fitted standard deviation. To address this, we restrict the Gaussian fit to a window of $\pm 25\%$ around the true M_{Z_D}. This strategy mitigates the impact of the tail while accurately capturing the core of the distribution; its validity is supported by the alignment of the distribution's peak with the true M_{Z_D}. The signal efficiency of this method is 52% for $M_{Z_\mathrm{D}} = 6$ TeV at 10 TeV MuC, and the other benchmarks have similar efficiency.

Figure 4 displays the extracted $\Delta m_{\mathrm{recoil}}$ and Δm_{ee} values as functions of M_{Z_D} for MuC energies of 3, 6, and 10 TeV. The Δm_{ee} values show negligible dependence on $\sqrt{s}$ within their respective kinematically allowed regions; for clarity, we therefore plot only the 10 TeV case.

Several key trends are apparent in the figure. At a given $\sqrt{s}$, $\Delta m_{\mathrm{recoil}}$ decreases with increasing M_{Z_D}. For a fixed M_{Z_D}, however, a higher collider energy $\sqrt{s}$ yields a larger $\Delta m_{\mathrm{recoil}}$, implying that the 3 TeV MuC offers better precision for masses within its kinematic reach. In contrast, Δm_{ee} increases with M_{Z_D}, reflecting the reduced detector performance for higher-energy electron pairs. Notably, the curves for Δm_{ee} and $\Delta m_{\mathrm{recoil}}$ at a given $\sqrt{s}$ intersect near $M_{Z_\mathrm{D}} \simeq \sqrt{s}/2$. This crossover suggests a natural division in the mass range, indicating which of the two observables is likely to be more powerful for discovery.

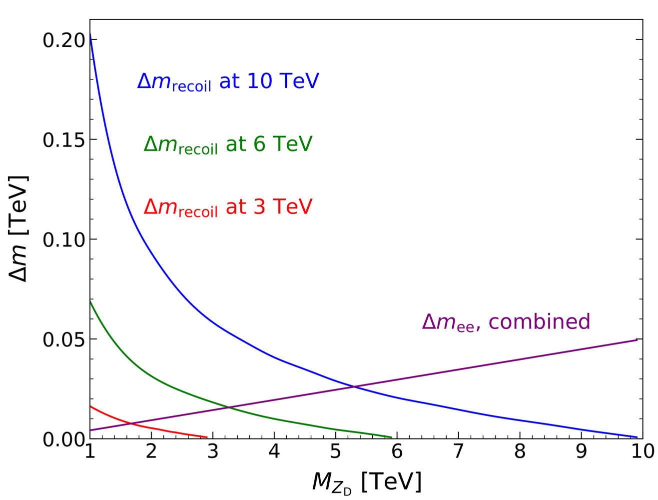

FIG. 4. $\Delta m_{\mathrm{recoil}}$ and Δm_{ee}, the standard deviations obtained from Gaussian fits to the m_{recoil} and m_{ee} distributions, as a function of M_{Z_D} at the 3 TeV, 6 TeV, and 10 TeV MuC.

In summary, the dependence of $\Delta m_{\mathrm{recoil}}$ and Δm_{ee} on both M_{Z_D} and $\sqrt{s}$ underscores the need for mass-dependent selection strategies when searching for heavy dark Z at a multi-TeV MuC. By applying appropriately tuned mass windows for different M_{Z_D} hypotheses, we can substantially enhance signal sensitivity.

IV. SIGNAL AND BACKGROUND ANALYSIS

In Sec. II, we identified two efficient discovery channels for the heavy Z_D at multi-TeV MuCs

$$\mu^+\mu^- \to Z_\mathrm{D}(\to jjX)\gamma, \tag{21}$$

$$\mu^+\mu^- \to Z_\mathrm{D}(\to e^+e^-)\gamma. \tag{22}$$

This section presents a comprehensive analysis of these channels, including background processes, simulation methodologies, and sensitivity projections.

A. Background processes and simulation methodology

The primary processes are $\mu^+\mu^- \to jj\gamma$ for the inclusive dijet mode and $\mu^+\mu^- \to e^+e^-\gamma$ for the e^+e^- mode. The limited detector coverage within $|\eta| < 2.5$ introduces additional background channels for both signal modes, including $\mu^+\mu^- \to W^+W^-\gamma$, $\mu^+\mu^- \to \tau^+\tau^-\gamma$, $\mu^+\mu^- \to t\bar{t}\gamma$, and $\mu^+\mu^- \to ZZ\gamma$.

To assess these background processes, we calculated their parton-level cross sections using MadGraph5-aMC@NLO [101] version 3.5.1, with the results presented in Table I. For each background at the 3, 6, and 10 TeV MuC energies, a sample of 5×10^5 events was generated. The following generator-level cuts were applied: all final-state photons, jets, electrons, and taus were required to be within $|\eta| < 2.5$. A minimum transverse momentum of $p_T > 20$ GeV was required for photons. For jets, electrons, and taus, an asymmetric p_T cut was imposed, with the leading particle (ordered by descending p_T) required to

TABLE I. Parton-level background cross sections at 3 TeV, 6 TeV, and 10 TeV MuCs. Cuts were applied requiring $p_T^\gamma > 20$ GeV, $p_T^{j_1,e_1,\tau_1} > 100$ GeV, $p_T^{j_2,e_2,\tau_2} > 20$ GeV, and $|\eta_{\gamma,j,e,\tau}| < 2.5$.

Background cross sections in units of fb			
Processes	$\sqrt{s} = 3$ TeV	$\sqrt{s} = 6$ TeV	$\sqrt{s} = 10$ TeV
$\mu^+\mu^- \to jj\gamma$	5.01×10	1.40×10	5.44
$\mu^+\mu^- \to e^+e^-\gamma$	9.31	2.75	1.10
$\mu^+\mu^- \to W^+W^-\gamma$	2.55×10	1.01×10	4.86
$\mu^+\mu^- \to \tau^+\tau^-\gamma$	5.37	1.63	6.67×10^{-1}
$\mu^+\mu^- \to t\bar{t}\gamma$	3.24	1.07	4.58×10^{-1}
$\mu^+\mu^- \to ZZ\gamma$	2.25	8.30×10^{-1}	3.82×10^{-1}

have $p_T > 100$ GeV and the subleading particle to have $p_T > 20$ GeV.

The results indicate that cross sections decrease with increasing c.m. energy across all background processes. The $\mu^+\mu^- \to jj\gamma$ process exhibits the highest cross section at all collision energies. Although $\mu^+\mu^- \to W^+W^-\gamma$ has the second-largest cross section, its contribution is to be suppressed by the branching ratios of $W \to jj$ or $W \to e\nu$. For the e^+e^- mode, $\mu^+\mu^- \to e^+e^-\gamma$ is the dominant background process. The $\mu^+\mu^- \to \tau^+\tau^-\gamma$ process has a slightly smaller cross section than $\mu^+\mu^- \to e^+e^-\gamma$ due to the heavier tau mass. The $\mu^+\mu^- \to t\bar{t}\gamma$ and $\mu^+\mu^- \to ZZ\gamma$ processes have relatively low cross sections.

We note that VBF processes can also contribute as potential background sources, namely the charged-current process $\mu^+\mu^- \to \nu_\mu\bar{\nu}_\mu Z\gamma$ and the neutral-current process $\mu^+\mu^- \to \mu^+\mu^- Z\gamma$. However, both channels exhibit distinct kinematic features that set them apart from the signal. The charged-current process is characterized by significant missing transverse energy E_T^{miss} from the final-state neutrinos—a feature absent in our signal—and can thus be suppressed by vetoing events with large E_T^{miss}. The neutral-current process produces highly energetic forward muons. Identification of these muons, whose momenta can peak around 2 TeV at a 10 TeV MuC [109], would be feasible using proposed forward muon detectors [55,72,116], enabling efficient rejection of such events. Given these powerful rejection methods, the VBF backgrounds were not included in our analysis.

Building on these parton-level insights, we performed fast detector simulations for both signal and background events using the Delphes framework. Jet reconstruction was carried out with the inclusive Valencia algorithm [117,118], implemented within the FastJet package [119], using a jet radius of $R = 0.5$ and a transverse-momentum threshold of $p_T > 20$ GeV. The Valencia algorithm is particularly well suited for high-energy lepton-collider environments, as its beam-jet concept effectively mitigates contamination from ISR photons and beam-induced backgrounds. For electrons and photons, we followed the default reconstruction settings of the Delphes muon-collider detector card (`delphes_card_MuonColliderDet.tcl`).

B. Inclusive two-jet signal analysis

We first analyze the inclusive dijet mode, $\mu^+\mu^- \to Z_D(\to jjX)\gamma$, implementing the following basic selection criteria for both signal and background events:

(i) Events must contain at least two jets ($N_j \geq 2$) and one photon ($N_\gamma \geq 1$), each with $p_T > 20$ GeV and $|\eta| < 2.5$.

(ii) The leading jet j_1 (ordered by descending p_T) must satisfy $p_T^{j_1} > 100$ GeV.

(iii) A lepton veto is applied, rejecting any event containing an electron or muon with $p_T > 20$ GeV and $|\eta| < 2.5$ (i.e., requiring $N_e = N_\mu = 0$).

The lepton veto ensures orthogonality between the dijet and e^+e^- samples, enabling an independent analysis of the two channels.

To optimize background suppression in the inclusive dijet mode, we examine two key kinematic observables: the photon recoil mass m_{recoil} and the leading jet invariant mass m_{j_1}. Figure 5 displays these distributions for both signal and backgrounds at the 3 TeV MuC after applying the basic selection. For the signal benchmarks, we set $\varepsilon = 0.01$ and examine M_{Z_D} values of 1, 2, and 2.7 TeV in the m_{recoil} distribution, while considering $M_{Z_D} = 1, 2.9$ TeV for the m_{j_1} distribution. The background contributions are presented as stacked histograms to facilitate direct comparison with the signal.

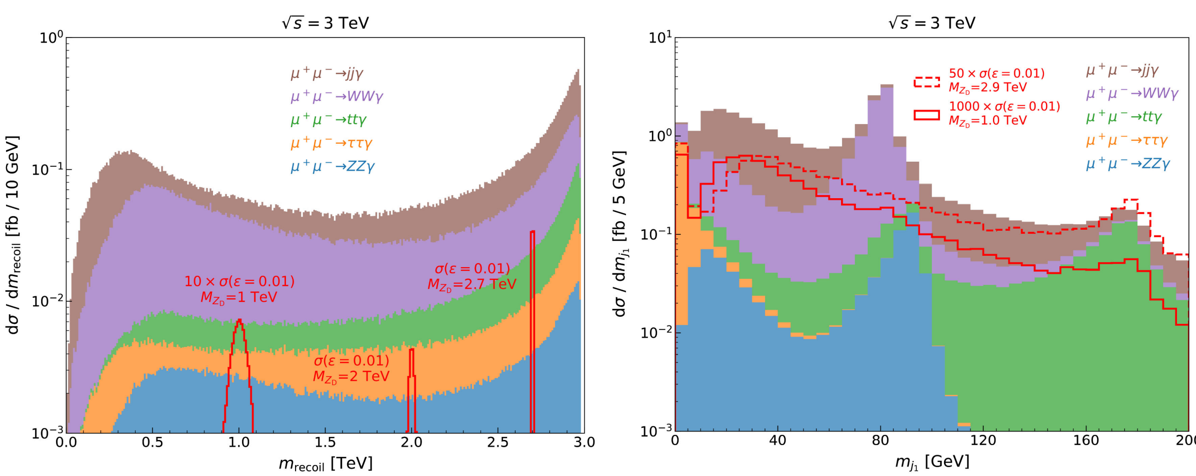

FIG. 5. Distributions of the recoil mass of the photon, m_{recoil}, (left) and the invariant mass of the leading jet, m_{j_1}, (right), for the signal and backgrounds at the 3 TeV MuC after basic selection. For the signal (red solid lines) with $\varepsilon = 0.01$, we consider $M_{Z_D} = 1$ TeV, 2 TeV, and 2.7 TeV in the m_{recoil} distribution, and $M_{Z_D} = 1$ TeV (solid) and 2.9 TeV (dashed) in the m_{j_1} distribution. Backgrounds are shown as stacked histograms for direct comparison.

The $m_{\rm recoil}$ distribution reveals distinct features between signal and background events. The signal shows a characteristic narrow peak that becomes sharper for higher $M_{Z_{\rm D}}$ values. In contrast, the background distributions remain nearly flat within the signal peak region. This clear distinction suggests an effective strategy: applying an optimized $m_{\rm recoil}$ cut around the signal peak.

The m_{j_1} distribution provides complementary discrimination power. For signal events, we observe substantial, nonzero, and smooth m_{j_1} values. In addition, the typical m_{j_1} increases with $M_{Z_{\rm D}}$, as illustrated by comparing the distributions for $M_{Z_{\rm D}} = 1$ TeV and 2.9 TeV. These features arise from the characteristic behavior of high-energy jets, where the differential cross section follows $d\sigma/dm_j^2 \sim \alpha_s/m_j^2 \ln(E_j^2/m_j^2)$ [120]. In contrast, the background m_{j_1} distributions exhibit distinctive peaks near m_W, m_Z, and m_t. These peaks originate from highly collimated decay products ($R < 0.4$) reconstructed as single jets from W, Z, and top quark decays, respectively. Among the background processes, the $\mu^+\mu^- \to W^+W^-\gamma$ channel produces the most prominent peak at $m_{j_1} \simeq m_W$. Therefore, vetoing events with m_{j_1} in the vicinity of m_W effectively suppresses this background contribution.

To quantify the effectiveness of our selection strategy, we present the cut-flow of cross sections for $\mu^+\mu^- \to Z_{\rm D}(\to jjX)\gamma$ at a 3 TeV MuC in Table II. This table also includes the signal significance $\mathcal{S}$, calculated for a total integrated luminosity of $\mathcal{L}_{\rm tot} = 1$ ab^{-1}, using the following formula [121]:

$$\mathcal{S} = \sqrt{2\left[(n_s + n_b)\ln\left(\frac{n_s + n_b}{n_b}\right) - n_s\right]}, \qquad (23)$$

where n_s and n_b denote the number of signal and background events, respectively.

For the detailed cut-flow analysis, we examine two benchmark points: $M_{Z_{\rm D}} = 1$ TeV and 2.7 TeV, both with $\varepsilon = 0.01$. Since the selection efficiencies up to the m_{j_1} cut are nearly identical for both masses, we present the complete cut-flow only for the $M_{Z_{\rm D}} = 1$ TeV case and show just the final result for $M_{Z_{\rm D}} = 2.7$ TeV to avoid repetition. All relevant background processes are included, with the exception of the negligible $\mu^+\mu^- \to ZZ\gamma$ channel.

The cut-flow results in Table II demonstrate the progressive improvement of our signal selection. After basic selection, the $jj\gamma$ and $W^+W^-\gamma$ backgrounds dominate, yielding a low initial signal significance of approximately 0.045σ. The W veto, defined by the requirement $|m_{j_1} - m_W| > 20$ GeV, is moderately effective and eliminates approximately 67% of the $W^+W^-\gamma$ background. The most substantial improvement comes from the $m_{\rm recoil}$ cut, which significantly suppresses all backgrounds while largely preserving the signal, demonstrating the power of the recoil mass as a discriminating variable.

The signal significance after the final selection based on the $m_{\rm recoil}$ variable is strongly dependent on the value of $M_{Z_{\rm D}}$. For the $M_{Z_{\rm D}} = 1$ TeV benchmark with $\varepsilon = 0.01$, the significance is only about 0.24σ, far below the detection threshold. In contrast, the heavier $M_{Z_{\rm D}} = 2.7$ TeV case shows a dramatic enhancement, reaching a significance of 3.96σ, which approaches the level required for discovery. This substantial improvement is a direct consequence of the superior mass resolution at higher masses; at the 3 TeV MuC, $\Delta m_{\rm recoil}$ improves from 16.3 GeV for $M_{Z_{\rm D}} = 1$ TeV to just 1.66 GeV for $M_{Z_{\rm D}} = 2.7$ TeV. Thus, for a fixed c.m. energy, heavier $Z_{\rm D}$ signal hypotheses achieve a higher discovery significance.

To explore the effects of higher c.m. energy, we extend our analysis to a 10 TeV MuC with an integrated luminosity of 10 ab^{-1}. The detailed cut-flow, showing cross sections and the resulting signal significance, is presented in Table III. As with the 3 TeV analysis, the negligible $ZZ\gamma$ background is omitted.

Our analysis at 10 TeV examines two benchmark hypotheses, $M_{Z_{\rm D}} = 1$ TeV and 9.7 TeV, both with $\varepsilon = 0.01$. The results show a striking contrast between the low-mass and high-mass scenarios. For the $M_{Z_{\rm D}} = 1$ TeV benchmark, the

TABLE II. Cut-flow of cross sections (in units of fb) and the corresponding significance for the signal process $\mu^+\mu^- \to Z_{\rm D}(\to jjX)\gamma$ with $\varepsilon = 0.01$ for $M_{Z_{\rm D}} = 1$ TeV and 2.7 TeV at the 3 TeV MuC. The significance $\mathcal{S}_{1\ {\rm ab}^{-1}}$ is calculated assuming a total integrated luminosity of 1 ab^{-1}. The basic selection criteria are described in the text, and note that the $\Delta m_{\rm recoil}$ and Δm_{ee} values depend on $M_{Z_{\rm D}}$.

Cut-flow of cross sections (fb) for $\mu^+\mu^- \to Z_{\rm D}(\to jjX)\gamma$ at a 3 TeV MuC with $\mathcal{L}_{\rm tot} = 1$ ab^{-1}						
$M_{Z_{\rm D}} = 1$ TeV and $\varepsilon = 0.01$						
Cut	$Z_{\rm D}(\to jj)\gamma$	$jj\gamma$	$W^+W^-\gamma$	$\tau^+\tau^-\gamma$	$t\bar{t}\gamma$	$\mathcal{S}_{1\ {\rm ab}^{-1}}$
Basic Selection	7.69×10^{-3}	1.42×10	1.15×10	1.08	1.86	4.47×10^{-2}
$\lvert m_{j_1} - m_W\rvert > 20$ GeV	6.34×10^{-3}	1.20×10	3.75	1.08	1.51	4.64×10^{-2}
$\lvert m_{\rm recoil} - M_{Z_{\rm D}}\rvert < 2\Delta m_{\rm recoil}$	3.47×10^{-3}	9.37×10^{-2}	8.47×10^{-2}	1.01×10^{-2}	1.29×10^{-2}	2.40×10^{-1}
$M_{Z_{\rm D}} = 2.7$ TeV and $\varepsilon = 0.01$						
$\lvert m_{\rm recoil} - M_{Z_{\rm D}}\rvert < 2\Delta m_{\rm recoil}$	3.12×10^{-2}	3.32×10^{-2}	6.22×10^{-3}	4.20×10^{-3}	7.72×10^{-3}	3.96

TABLE III. Cut-flow of the cross sections (in units of fb) and the corresponding significance for the signal process $\mu^+\mu^- \to Z_D(\to jjX)\gamma$ with $\varepsilon = 0.01$ and $M_{Z_D} = 1, 9.7$ TeV at the 10 TeV MuC. The significance $\mathcal{S}_{10\ \mathrm{ab}^{-1}}$ is calculated assuming a total integrated luminosity of 10 ab^{-1}. The basic selection criteria are described in the text, and note that the $\Delta m_{\mathrm{recoil}}$ and Δm_{ee} values depend on M_{Z_D}.

Cut-flow of cross sections [fb] for $\mu^+\mu^- \to Z_D(\to jjX)\gamma$ at a 10 TeV MuC with $\mathcal{L}_{\mathrm{tot}} = 10\ \mathrm{ab}^{-1}$						
$M_{Z_D} = 1$ TeV and $\varepsilon = 0.01$						
Cut	$Z_D(\to jj)\gamma$	$jj\gamma$	$W^+W^-\gamma$	$\tau^+\tau^-\gamma$	$t\bar{t}\gamma$	$\mathcal{S}_{10\ \mathrm{ab}^{-1}}$
Basic Selection	5.09×10^{-4}	1.21	1.86	1.37×10^{-1}	2.91×10^{-1}	2.69×10^{-2}
$\lvert m_{j_1} - m_W \rvert > 20$ GeV	4.02×10^{-4}	9.25×10^{-1}	5.14×10^{-1}	1.33×10^{-1}	2.78×10^{-1}	2.93×10^{-2}
$\lvert m_{\mathrm{recoil}} - M_{Z_D} \rvert < 2\Delta m_{\mathrm{recoil}}$	2.28×10^{-4}	4.55×10^{-2}	9.00×10^{-2}	4.49×10^{-3}	9.23×10^{-3}	5.85×10^{-2}
$M_{Z_D} = 9.7$ TeV and $\varepsilon = 0.01$						
$\lvert m_{\mathrm{recoil}} - M_{Z_D} \rvert < 2\Delta m_{\mathrm{recoil}}$	1.18×10^{-2}	3.18×10^{-3}	9.43×10^{-4}	3.95×10^{-4}	1.20×10^{-3}	12.4

final significance is just 0.058σ at 10 TeV, illustrating the challenge of probing low-mass states at higher-energy colliders. Conversely, the $M_{Z_D} = 9.7$ TeV search demonstrates the unique potential of high-energy MuCs, achieving a significance of 12.4σ. This remarkable improvement stems from a combination of three factors: a larger signal cross section (see Fig. 1); a much-improved mass resolution $\Delta m_{\mathrm{recoil}}$ (see Fig. 4); and the ten-fold increase in integrated luminosity. These results underscore the complementarity of different collider energies for exploring the M_{Z_D} parameter space, with high-energy MuCs excelling at searches for heavy new particles.

C. Analysis of the $Z_D \to e^+e^-$ channel

We now analyze the e^+e^- mode, $\mu^+\mu^- \to Z_D(\to e^+e^-)\gamma$, beginning with the application of the following basic selection criteria:

(i) Events must contain exactly two electrons ($N_e = 2$) and at least one photon ($N_\gamma \geq 1$), each satisfying $p_T > 20$ GeV and $|\eta| < 2.5$.

(ii) The leading electron e_1 (ordered by descending p_T) is required to have $p_T^{e_1} > 100$ GeV.

(iii) A jet and muon veto is applied, rejecting any event that contains a jet or a muon with $p_T > 20$ GeV and $|\eta| < 2.5$ (i.e., requiring $N_j = N_\mu = 0$).

This veto ensures that the e^+e^- sample is distinct and orthogonal to the inclusive dijet sample.

To optimize our background suppression strategy in the e^+e^- mode, we examine two key kinematic observables: the invariant mass of the electron-positron pair (m_{ee}) and the total energy of the $e^+e^-\gamma$ system ($E_{ee\gamma}$). Figure 6 presents these distributions for both signal and backgrounds at the 3 TeV MuC after applying the basic selection. Note that the recoil mass distribution is nearly identical to that in the jjX mode, as shown in Fig. 5. In Fig. 6, we consider the signal with $\varepsilon = 0.01$ for three mass hypotheses ($M_{Z_D} = 1, 2, 2.7$ TeV) in the m_{ee} distribution and two mass hypotheses ($M_{Z_D} = 1, 2.7$ TeV) in the $E_{ee\gamma}$ distribution.

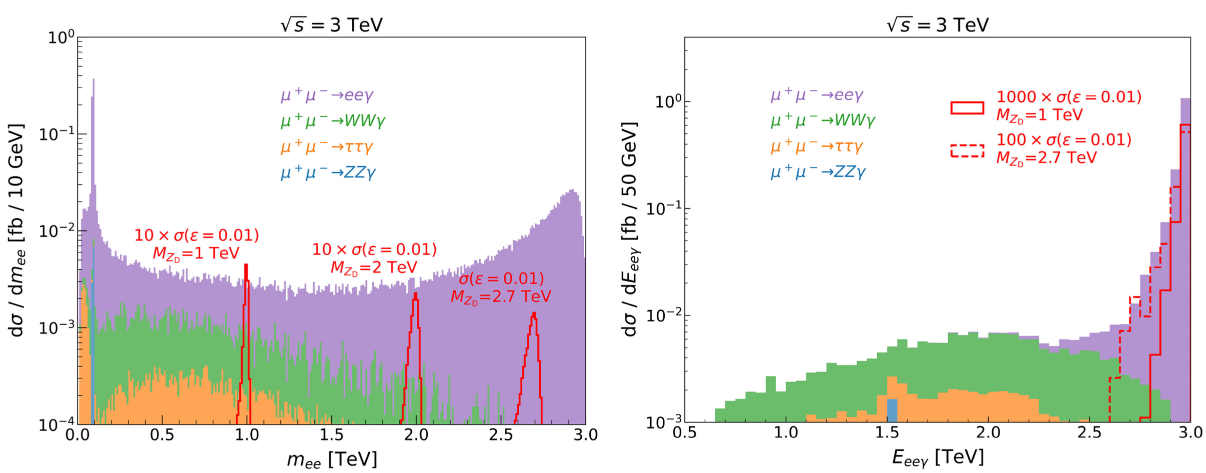

FIG. 6. Distributions of the invariant mass of the e^+e^- pair (left) and the total energy of the $e^+e^-\gamma$ system, $E_{ee\gamma}$, (right) for the signal and backgrounds at the 3 TeV MuC after the basic selection. For the signal (red solid lines), we set $\varepsilon = 0.01$ and consider $M_{Z_D} = 1, 2, 2.7$ TeV for the m_{ee} distribution, and $M_{Z_D} = 1, 2.7$ TeV for the $E_{ee\gamma}$ distribution. Backgrounds are shown as stacked histograms for direct comparison.

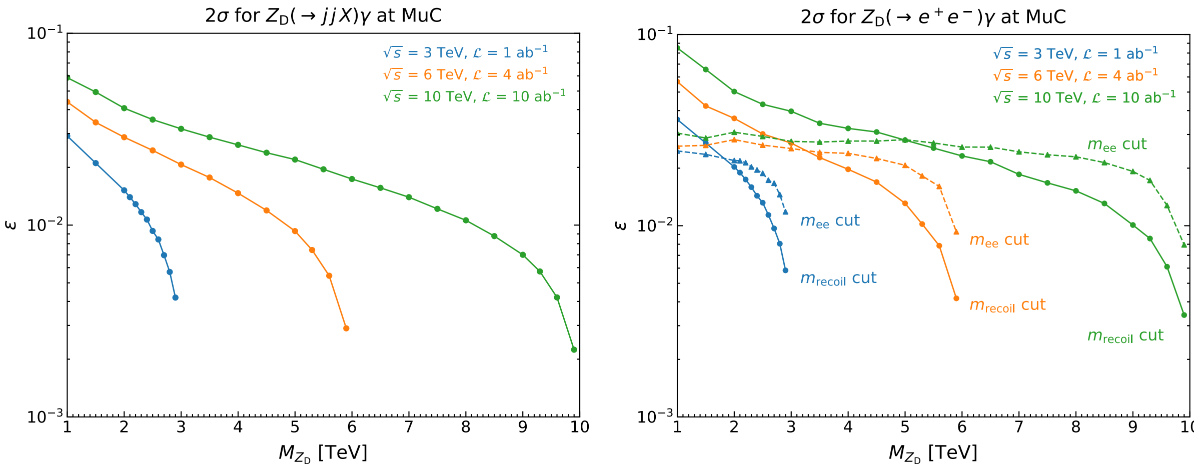

FIG. 7. 2σ sensitivity contours for detecting a dark Z boson at different MuC energies through the processes $\mu^+\mu^- \to Z_D(\to jjX)\gamma$ (left) and $\mu^+\mu^- \to Z_D(\to e^+e^-)\gamma$ (right). The results for the 3 TeV MuC with $\mathcal{L}_{tot} = 1\ \mathrm{ab}^{-1}$, 6 TeV MuC with $\mathcal{L}_{tot} = 4\ \mathrm{ab}^{-1}$, and 10 TeV MuC with $\mathcal{L}_{tot} = 10\ \mathrm{ab}^{-1}$ are shown in blue, orange, and green, respectively. For the e^+e^- mode, solid lines denote results based on the m_{recoil} cut, while dashed lines denote those based on the m_{ee} cut.

The m_{ee} distribution exhibits clear signal features: a resonance peak of which the width increases with M_{Z_D}. In contrast, the background m_{ee} distribution remains smooth across the signal region, indicating that a narrow m_{ee} cut can effectively suppress background while preserving signal efficiency.

The $E_{ee\gamma}$ distribution reveals another distinctive feature: both the signal and the irreducible background ($\mu^+\mu^- \to e^+e^-\gamma$) peak at $\sqrt{s}$. This behavior occurs because these processes produce only $e^+e^-\gamma$ in the final state, retaining most of the collision energy despite small losses to FSR. In contrast, reducible background processes, which produce additional particles, exhibit significant energy loss in the $e^+e^-\gamma$ system. This characteristic suggests that requiring $E_{ee\gamma} > 0.9\sqrt{s}$ would efficiently suppress all the reducible backgrounds.

To quantify the impact of the $E_{ee\gamma}$ cut, we present a preliminary cut-flow analysis in Table IV for the process $\mu^+\mu^- \to Z_D(\to e^+e^-)\gamma$ at a 3 TeV MuC with $\mathcal{L}_{tot} = 1\ \mathrm{ab}^{-1}$. We examine two benchmark points with $\varepsilon = 0.01$: $M_{Z_D} = 1$ TeV and $M_{Z_D} = 2.7$ TeV. After the basic selection, the irreducible background $\mu^+\mu^- \to e^+e^-\gamma$ dominates, exceeding the signal by factors of approximately 1000 and 100 for $M_{Z_D} = 1$ TeV and $M_{Z_D} = 2.7$ TeV, respectively. The reducible background $\mu^+\mu^- \to W^+W^-\gamma$ also exceeds the signal, although it is smaller than the irreducible contribution. The $E_{ee\gamma} > 0.9\sqrt{s}$ cut proves highly effective in suppressing the reducible $\mu^+\mu^- \to W^+W^-\gamma$ background, reducing its cross section by approximately 94%.

With the preliminary cuts established, a crucial question arises: should we apply a cut on m_{recoil}, m_{ee}, or both? The choice is nontrivial since the optimized mass window cuts for m_{recoil} and m_{ee} show opposite behaviors with respect to M_{Z_D}. For a comparative analysis of these final selection strategies, Table V presents the signal significance of three different final selections: (1) m_{recoil} cut only, (2) m_{ee} cut only, and (3) combined cut applying both conditions. The basic selection and $E_{ee\gamma} > 0.9\sqrt{s}$ cut from Table IV have been applied.

For lighter Z_D ($M_{Z_D} = 1$ TeV), the m_{ee} cut alone proves most efficient, yielding a significance 2.2 times that achieved with the m_{recoil} cut alone. This aligns with the opposite behavior of Δm_{recoil} and Δm_{ee} with respect to

TABLE IV. Preliminary cut-flow of cross sections (in units of fb) for the signal process $\mu^+\mu^- \to Z_D(\to e^+e^-)\gamma$ with $\varepsilon = 0.01$ for $M_{Z_D} = 1$ TeV and 2.7 TeV at the 3 TeV MuC. The significance $\mathcal{S}_{1\ \mathrm{ab}^{-1}}$ is calculated assuming an integrated luminosity of 1 ab^{-1} and the basic selection criteria are described in the text.

Preliminary cut-flow of cross sections [fb] for $\mu^+\mu^- \to Z_D(\to e^+e^-)\gamma$ at a 3 TeV MuC with $\mathcal{L}_{tot} = 1\ \mathrm{ab}^{-1}$						
	Backgrounds		$M_{Z_D} = 1$ TeV		$M_{Z_D} = 2.7$ TeV	
Cut	$e^+e^-\gamma$	$W^+W^-\gamma$	$Z_D(\to e^+e^-)\gamma$	$\mathcal{S}_{1\ \mathrm{ab}^{-1}}$	$Z_D(\to e^+e^-)\gamma$	$\mathcal{S}_{1\ \mathrm{ab}^{-1}}$
Basic Selection	2.14	1.32×10^{-1}	1.10×10^{-3}	2.28×10^{-2}	1.07×10^{-2}	2.22×10^{-1}
$E_{ee\gamma} > 0.9\sqrt{s}$	2.11	7.85×10^{-3}	1.09×10^{-3}	2.37×10^{-2}	1.06×10^{-2}	2.30×10^{-1}

TABLE V. Signal cross sections and significances for $\mu^+\mu^- \to Z_D(\to e^+e^-)\gamma$ at a 3 TeV MuC with $\mathcal{L}_{\rm tot} = 1$ ab^{-1}, shown for $M_{Z_D} = 1$ TeV and $M_{Z_D} = 2.7$ TeV. We fixed $\varepsilon = 0.01$. Results are presented after basic selection, $E_{ee\gamma} > 0.9\sqrt{s}$ cut, and three final selection criteria: (i) $m_{\rm recoil}$ cut; (ii) m_{ee} cut; (iii) combined cut applying both conditions.

Final selection results for $\mu^+\mu^- \to Z_D(\to e^+e^-)\gamma$ at a 3 TeV MuC with $\mathcal{L}_{\rm tot} = 1$ ab^{-1}						
	$m_{\rm recoil}$ cut		m_{ee} cut		Combined	
	$\sigma_{\rm sig}$ [fb]	$\mathcal{S}_{1\ {\rm ab}^{-1}}$	$\sigma_{\rm sig}$ [fb]	$\mathcal{S}_{1\ {\rm ab}^{-1}}$	$\sigma_{\rm sig}$ [fb]	$\mathcal{S}_{1\ {\rm ab}^{-1}}$
$M_{Z_D} = 1$ TeV	6.01×10^{-4}	1.69×10^{-1}	6.88×10^{-4}	3.75×10^{-1}	3.79×10^{-4}	3.04×10^{-1}
$M_{Z_D} = 2.7$ TeV	5.91×10^{-3}	2.12	5.71×10^{-3}	7.37×10^{-1}	3.23×10^{-3}	1.61

M_{Z_D}, as illustrated in Fig. 4. Notably, the m_{ee} cut also outperforms the combined cut, achieving a significance about 20% higher.

For heavier Z_D ($M_{Z_D} = 2.7$ TeV), the situation reverses. The $m_{\rm recoil}$ cut alone is most effective, achieving a significance of approximately 2.41σ for $\varepsilon = 0.01$. This value is 2.9 times that obtained with the m_{ee} cut alone and 1.4 times that achieved with the combined cut.

D. Combined results

In this final subsection, we present comprehensive results of 2σ and 5σ sensitivity projections in the (M_{Z_D}, ε) parameter space by combining the inclusive dijet and e^+e^- modes. Our analysis is based on detector-level simulations, as described in the previous sections. To systematically explore the parameter space, we selected 12, 12, and 20 benchmark values of M_{Z_D} for the 3, 6, and 10 TeV MuC configurations, respectively, all at a fixed coupling of $\varepsilon = 0.01$. For each M_{Z_D} benchmark point, we generated 5×10^4 signal events. Since ε affects only the total signal rate while preserving the distribution shapes, we can efficiently explore the full (M_{Z_D}, ε) parameter space by scaling the signal cross section according to ε^2.

We first present the 2σ sensitivity contours in Fig. 7, shown separately for the $Z_D \to jjX$ mode (left panel) and $Z_D \to e^+e^-$ mode (right panel). We examine three MuC configurations: $\sqrt{s} = 3$ TeV with $\mathcal{L}_{\rm tot} = 1$ ab^{-1} (blue), $\sqrt{s} = 6$ TeV with $\mathcal{L}_{\rm tot} = 4$ ab^{-1} (orange), and $\sqrt{s} = 10$ TeV with $\mathcal{L}_{\rm tot} = 10$ ab^{-1} (green).

For the jjX mode, the results are based on the cut-flow outlined in Table II. Our analysis reveals two universal trends. First, the ε sensitivity limit as a function of M_{Z_D} exhibits a consistent shape across all c.m. energies, improving rapidly with increasing M_{Z_D}. This enhancement stems from the increasing cross section and tighter $m_{\rm recoil}$ cuts for heavier M_{Z_D}. Second, the ε sensitivity extends to higher M_{Z_D} values as the collision energy increases, a direct consequence of the expanded kinematic phase space.

For the e^+e^- mode, we present two sets of results: one based on the $m_{\rm recoil}$ cut (solid lines) and another on the m_{ee} cut (dashed lines). Both cuts yield similar trends in ε sensitivity, improving as M_{Z_D} increases. The m_{ee} cut enhances ε sensitivity for heavier M_{Z_D}, even though our optimized cut on the m_{ee} distribution becomes weaker. This is primarily due to the increased signal cross section for heavier Z_D masses, as shown in Fig. 1.

Although the overall sensitivity trend as a function of M_{Z_D} is similar for selections based on either $m_{\rm recoil}$ or m_{ee}, their quantitative performance differs significantly across the mass range. For lighter M_{Z_D} values, the m_{ee} selection consistently outperforms the $m_{\rm recoil}$ selection at all collider energies. For $M_{Z_D} = 1$ TeV at the 3 TeV MuC, applying the m_{ee} cut improves the 2σ sensitivity limit on ε to 0.025, compared to 0.036 from the $m_{\rm recoil}$ cut. This advantage is even more pronounced at 10 TeV, where the m_{ee} selection limit of $\varepsilon \simeq 0.030$ is approximately 2.8 times stronger than the $m_{\rm recoil}$ selection's limit of $\varepsilon \simeq 0.085$. These results clearly demonstrate the superiority of the m_{ee}-based selection for probing the low-mass Z_D regime. Conversely, for heavier M_{Z_D} values, the $m_{\rm recoil}$ selection becomes more effective.

An interesting observation is that the 2σ sensitivity contours for the m_{ee} and $m_{\rm recoil}$ selections intersect near $M_{Z_D} \simeq \sqrt{s}/2$. Based on this feature, we implement the m_{ee} selection for $M_{Z_D} < \sqrt{s}/2$ and the $m_{\rm recoil}$ selection for $M_{Z_D} > \sqrt{s}/2$ in the e^+e^- mode.

Finally, we combine the two processes, $\mu^+\mu^- \to Z_D(\to jjX)\gamma$ and $\mu^+\mu^- \to Z_D(\to e^+e^-)\gamma$. Statistical independence between the two measurements is ensured by the lepton veto in the inclusive dijet channel and the jet veto in the e^+e^- mode. Assuming the two processes are independent, the combined significance can be expressed as $\mathcal{S}_{\rm tot} = \sqrt{\mathcal{S}_{jjX}^2 + \mathcal{S}_{ee}^2}$, where $\mathcal{S}_{jjX}$ ($\mathcal{S}_{ee}$) denotes the significance from the jjX (e^+e^-) mode. This approach enables efficient computation of the 2σ and 5σ sensitivity limits across the entire parameter space.

Figure 8 presents our final combined sensitivity for the jjX and e^+e^- modes. The solid and dashed lines respectively show the 2σ and 5σ sensitivity contours as a function of M_{Z_D}. The results for the MuC configurations at 3 TeV ($\mathcal{L}_{\rm tot} = 1$ ab^{-1}), 6 TeV ($\mathcal{L}_{\rm tot} = 4$ ab^{-1}), and 10 TeV ($\mathcal{L}_{\rm tot} = 10$ ab^{-1}) are shown in blue, orange, and green, respectively. For comparison, we also plot the projected 2σ sensitivity limits from studies of the HL-LHC

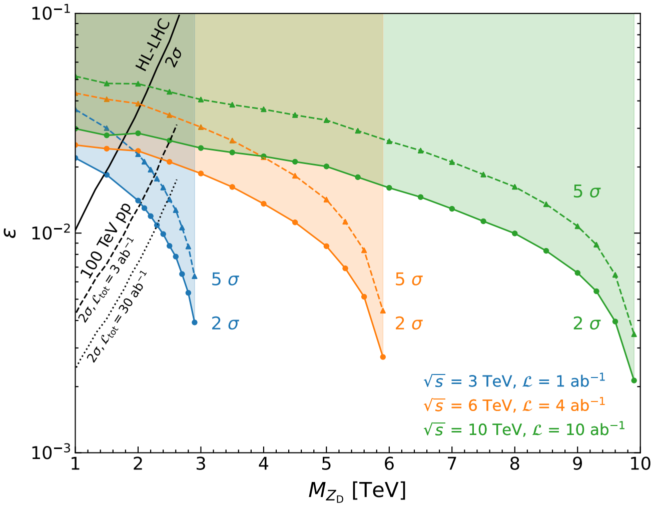

FIG. 8. 2σ (solid lines) and 5σ (dashed lines) sensitivity contours for detecting a dark Z boson at different MuC energies, combining the processes $\mu^+\mu^- \to Z_D(\to jjX)\gamma$ and $\mu^+\mu^- \to Z_D(\to e^+e^-)\gamma$. The results for the 3 TeV MuC with $\mathcal{L}_{tot} = 1\ \text{ab}^{-1}$, 6 TeV with $\mathcal{L}_{tot} = 4\ \text{ab}^{-1}$, and 10 TeV with $\mathcal{L}_{tot} = 10\ \text{ab}^{-1}$ are shown in blue, orange, and green, respectively. The 2σ sensitivity limit of ε at the HL-LHC ($\sqrt{s} = 14$ TeV, $\mathcal{L}_{tot} = 3\ \text{ab}^{-1}$) and at a 100 TeV pp collider ($\mathcal{L}_{tot} = 3\ \text{ab}^{-1}$ and $\mathcal{L}_{tot} = 30\ \text{ab}^{-1}$) are also shown.

($\sqrt{s} = 14$ TeV, $\mathcal{L}_{tot} = 3\ \text{ab}^{-1}$) and a 100 TeV pp collider [45]. Projections for the 100 TeV collider are shown for integrated luminosities of both 3 ab^{-1} and 30 ab^{-1}. The latter projection, which corresponds to the canonical luminosity target for a future collider [122], is derived by rescaling the 3 ab^{-1} limit.

Our analysis demonstrates that combining different decay modes slightly enhances the sensitivity to ε. For $M_{Z_D} = 1$ TeV at the 3 TeV MuC, while the e^+e^- decay mode alone can probe down to $\varepsilon = 2.46 \times 10^{-2}$ at 2σ significance, combining the jjX and e^+e^- modes improves this limit to $\varepsilon = 2.19 \times 10^{-2}$, representing an 11% enhancement in sensitivity. At the 6 TeV and 10 TeV MuC, combining the two channels for $M_{Z_D} = 1$ TeV yields more modest improvements of approximately 3.5% and 2%, respectively.

For the heaviest accessible cases ($M_{Z_D} = \sqrt{s} - 100$ GeV) at each collision energy, combining both channels allows us to reach $\varepsilon = 3.9 \times 10^{-3}$ at the 3 TeV MuC, $\varepsilon = 2.7 \times 10^{-3}$ at the 6 TeV MuC, and $\varepsilon = 2.1 \times 10^{-3}$ at the 10 TeV MuC. Relative to the ε sensitivity limit in the e^+e^- mode alone (see Fig. 7), the addition of the inclusive dijet mode improves the sensitivity by approximately 6.4%, 5.8%, and 4.8% at the 3 TeV, 6 TeV, and 10 TeV MuC, respectively.

Finally, we compare our results with the sensitivity projections for the HL-LHC ($\sqrt{s} = 14$ TeV, $\mathcal{L}_{tot} = 3\ \text{ab}^{-1}$) and a 100 TeV pp collider ($\mathcal{L}_{tot} = 3\ \text{ab}^{-1}, 30\ \text{ab}^{-1}$) [45]. For $M_{Z_D} = 1$ TeV, the HL-LHC can achieve a sensitivity limit of $\varepsilon \simeq 10^{-2}$, while the 100 TeV pp collider reaches $\varepsilon \simeq 2.1 \times 10^{-3} (4.3 \times 10^{-3})$ for $\mathcal{L}_{tot} = 30\ \text{ab}^{-1} (\mathcal{L}_{tot} = 3\ \text{ab}^{-1})$. For this relatively light M_{Z_D}, both hadron colliders outperform the MuC.

However, as M_{Z_D} increases, the MuC demonstrates significant advantages. Compared to the 3 TeV MuC, the HL-LHC achieves similar ε sensitivity at $M_{Z_D} = 1.5$ TeV, while a 100 TeV pp collider reaches this level at $M_{Z_D} = 2$ TeV (with $\mathcal{L}_{tot} = 3\ \text{ab}^{-1}$) and at $M_{Z_D} = 2.4$ TeV (with $\mathcal{L}_{tot} = 30\ \text{ab}^{-1}$). Beyond these mass points, the sensitivity of both hadron colliders deteriorates rapidly, with their reach limited to $M_{Z_D} \lesssim 2.7$ TeV. In contrast, the multi-TeV MuC becomes increasingly effective at probing heavier M_{Z_D} values within its kinematic reach. This superior performance persists across different MuC energies.

V. CONCLUSIONS

In this study, we have explored the discovery potential of multi-TeV muon colliders (MuCs) for a heavy dark Z boson (Z_D) through the associated production channel $\mu^+\mu^- \to Z_D\gamma$. This production mechanism is central to our approach, as it enables precise M_{Z_D} reconstruction through the recoil mass technique with well-measured photon energy. We focused on two decay modes, $Z_D \to jjX$ and $Z_D \to e^+e^-$, and demonstrated that MuCs operating at 3, 6, and 10 TeV with integrated luminosities of 1, 4, and 10 ab^{-1}, respectively, can significantly improve sensitivity to the kinetic mixing parameter ε over a broad Z_D mass range—particularly above 1 TeV—compared to hadron colliders.

A key advancement in our analysis is the implementation of M_{Z_D}-dependent cuts on both the recoil mass (m_{recoil}) and the electron-positron invariant mass (m_{ee}). Instead of employing fixed mass windows, our cuts are guided by detector resolutions, Δm_{recoil} and Δm_{ee}, which we determined as a function of both M_{Z_D} and $\sqrt{s}$. This approach accounts for the crucial fact that detector resolution degrades for more energetic particles.

This energy dependence creates a powerful complementarity between the two analysis strategies. A lighter Z_D yields a highly energetic photon, enhancing Δm_{recoil}, but produces a less energetic e^+e^- pair, reducing Δm_{ee}. Consequently, the m_{ee}-based selection is superior for lower Z_D masses, while the m_{recoil}-based selection becomes more effective for heavier ones. Our optimized strategy leverages this trade-off by applying an increasingly stringent m_{recoil} cut for heavy Z_D signals, which is key to achieving high sensitivity. For the $Z_D \to e^+e^-$ channel, we identified a natural crossover in performance near $M_{Z_D} \simeq \sqrt{s}/2$ in the $Z_D \to e^+e^-$ channel, allowing us to deploy the optimal selection in each mass regime and thereby maximize the discovery potential across the entire spectrum.

The combination of jjX and e^+e^- decay channels further improves the overall sensitivity. While for

$M_{Z_D} \lesssim 2$ TeV, the sensitivity gains at MuCs are comparable to those at the HL-LHC or a 100 TeV pp collider, our strategy achieves ε sensitivity down to $\mathcal{O}(10^{-3})$ as M_{Z_D} approaches $\sqrt{s}$, substantially outperforming any future hadron colliders. These results demonstrate the fundamental advantages of MuCs—the ability to fully exploit the c.m. energy and provide cleaner final states.

Looking ahead, these findings underscore the promise of MuCs in probing heavy dark sectors that remain inaccessible at hadron colliders. The photon recoil mass technique remains effective even when Z_D decays into dark sector particles. As detector simulations, reconstruction algorithms, and statistical tools continue to advance, MuCs will likely achieve even greater sensitivity. These developments establish the multi-TeV MuC as a pivotal facility for deepening our understanding of the dark sector.

ACKNOWLEDGMENTS

We thank Dr. Adil Jueid and Dr. Daohan Wang for useful discussions. The work of K. C. is supported by National Science and Technology Council (NSTC) 113-2112-M-007-041-MY3. The work of P. S. is supported by Basic Science Research Program through the National Research Foundation of Korea (NRF) funded by the Ministry of Education through the Center for Quantum Spacetime (CQUeST) of Sogang University (No. RS-2020-NR049598). The work of J. S. is supported by the National Research Foundation of Korea, Grant No. NRF-2022R1A2C1007583. J. K. supported by a KIAS Individual Grant (No. PG099201) at Korea Institute for Advanced Study. The work of S. L. is supported by Basic Science Research Program through the National Research Foundation of Korea (NRF) funded by the Ministry of Education (No. RS-2023-00274098).

DATA AVAILABILITY

The data that support the findings of this article are not publicly available. The data are available from the authors upon reasonable request.

[1] G. Aad *et al.* (ATLAS Collaboration), Observation of a new particle in the search for the standard model Higgs boson with the ATLAS detector at the LHC, Phys. Lett. B **716**, 1 (2012).

[2] S. Chatrchyan *et al.* (CMS Collaboration), Observation of a new boson at a mass of 125 GeV with the CMS experiment at the LHC, Phys. Lett. B **716**, 30 (2012).

[3] L. B. Okun, Limits of electrodynamics: Paraphotons?, Sov. Phys. JETP **56**, 502 (1982).

[4] B. Holdom, Two U(1)'s and epsilon charge shifts, Phys. Lett. **166B**, 196 (1986).

[5] P. Fayet, Extra U(1)'s and new forces, Nucl. Phys. **B347**, 743 (1990).

[6] M. Fabbrichesi, E. Gabrielli, and G. Lanfranchi, *The Physics of the Dark Photon* (Springer, Cham, 2021).

[7] P. Galison and A. Manohar, Two Z's or not two Z's? Phys. Lett. **136B**, 279 (1984).

[8] J. H. Chang, R. Essig, and S. D. McDermott, Revisiting supernova 1987A constraints on dark photons, J. High Energy Phys. 01 (2017) 107.

[9] A. Bross, M. Crisler, S. H. Pordes, J. Volk, S. Errede, and J. Wrbanek, A search for shortlived particles produced in an electron beam dump, Phys. Rev. Lett. **67**, 2942 (1991).

[10] S. N. Gninenko, Constraints on sub-GeV hidden sector gauge bosons from a search for heavy neutrino decays, Phys. Lett. B **713**, 244 (2012).

[11] J. Blumlein and J. Brunner, New exclusion limits for dark gauge forces from beam-dump data, Phys. Lett. B **701**, 155 (2011).

[12] J. Blümlein and J. Brunner, New exclusion limits on dark gauge forces from proton bremsstrahlung in beam-dump data, Phys. Lett. B **731**, 320 (2014).

[13] E. M. Riordan *et al.*, A search for short lived axions in an electron beam dump experiment, Phys. Rev. Lett. **59**, 755 (1987).

[14] D. Banerjee *et al.*, Search for invisible decays of sub-GeV dark photons in missing-energy events at the CERN SPS, Phys. Rev. Lett. **123**, 121801 (2019).

[15] J. R. Batley *et al.* (NA48/2 Collaboration), Search for the dark photon in π^0 decays, Phys. Lett. B **746**, 178 (2015).

[16] M. Pospelov, Secluded U(1) below the weak scale, Phys. Rev. D **80**, 095002 (2009).

[17] J. R. Batley *et al.* (NA48/2 Collaboration), Search for the dark photon in π^0 decays, Phys. Lett. B **746**, 178 (2015).

[18] H. Merkel *et al.*, Search at the mainz microtron for light massive gauge bosons relevant for the muon g-2 anomaly, Phys. Rev. Lett. **112**, 221802 (2014).

[19] J. P. Lees *et al.* (*BABAR* Collaboration), Search for a dark photon in e^+e^- collisions at *BABAR*, Phys. Rev. Lett. **113**, 201801 (2014).

[20] F. Archilli *et al.* (KLOE-2 Collaboration), Search for a vector gauge boson in ϕ meson decays with the KLOE detector, Phys. Lett. B **706**, 251 (2012).

[21] D. Babusci *et al.* (KLOE-2 Collaboration), Limit on the production of a light vector gauge boson in phi meson decays with the KLOE detector, Phys. Lett. B **720**, 111 (2013).

[22] R. Aaij *et al.* (LHCb Collaboration), Search for dark photons produced in 13 TeV pp collisions, Phys. Rev. Lett. **120**, 061801 (2018).
[23] W. Altmannshofer *et al.* (Belle-II Collaboration), The Belle II Physics book, Prog. Theor. Exp. Phys. **2019**, 123C01 (2019); **2020**, 029201(E) (2020).
[24] P. Ilten, Y. Soreq, J. Thaler, M. Williams, and W. Xue, Proposed inclusive dark photon search at LHCb, Phys. Rev. Lett. **116**, 251803 (2016).
[25] P. Ilten, J. Thaler, M. Williams, and W. Xue, Dark photons from charm mesons at LHCb, Phys. Rev. D **92**, 115017 (2015).
[26] J. D. Bjorken, S. Ecklund, W. R. Nelson, A. Abashian, C. Church, B. Lu *et al.*, Search for neutral metastable penetrating particles produced in the SLAC beam dump, Phys. Rev. D **38**, 3375 (1988).
[27] B. Batell, R. Essig, and Z. Surujon, Strong constraints on Sub-GeV dark sectors from SLAC beam dump E137, Phys. Rev. Lett. **113**, 171802 (2014).
[28] L. Marsicano, M. Battaglieri, M. Bondi', C. D. R. Carvajal, A. Celentano, M. De Napoli, R. De Vita, E. Nardi, M. Raggi, and P. Valente, Dark photon production through positron annihilation in beam-dump experiments, Phys. Rev. D **98**, 015031 (2018).
[29] F. Bergsma *et al.* (CHARM Collaboration), Search for axion like particle production in 400-GeV proton—copper interactions, Phys. Lett. **157B**, 458 (1985).
[30] J. Beacham *et al.*, Physics beyond colliders at CERN: Beyond the standard model working group report, J. Phys. G **47**, 010501 (2020).
[31] S. Martellotti, The NA62 experiment at CERN, arXiv:1510.00172.
[32] J.L. Feng, I. Galon, F. Kling, and S. Trojanowski, ForwArd Search ExpeRiment at the LHC, Phys. Rev. D **97**, 035001 (2018).
[33] K. Cheung and C. J. Ouseph, Sensitivities on dark photon from the forward physics experiments, J. High Energy Phys. 10 (2022) 196.
[34] A. Berlin, S. Gori, P. Schuster, and N. Toro, Dark sectors at the Fermilab SeaQuest experiment, Phys. Rev. D **98**, 035011 (2018).
[35] P. H. Adrian *et al.* (HPS Collaboration), Search for a dark photon in electroproduced e^+e^- pairs with the Heavy Photon Search experiment at JLab, Phys. Rev. D **98**, 091101 (2018).
[36] A. Caldwell *et al.*, Particle physics applications of the AWAKE acceleration scheme, arXiv:1812.11164.
[37] L. Doria, P. Achenbach, M. Christmann, A. Denig, and H. Merkel, Dark matter at the intensity frontier: The new MESA electron accelerator facility, Proc. Sci. ALPS2019 (**2020**) 022 [arXiv:1908.07921].
[38] L. Doria, P. Achenbach, M. Christmann, A. Denig, P. Gülker, and H. Merkel, Search for light dark matter with the MESA accelerator, in *13th Conference on the Intersections of Particle and Nuclear Physics* (2018), 9, arXiv:1809.07168.
[39] CMS Collaboration, Search for a narrow resonance decaying to a pair of muons in proton-proton collisions at 13 TeV, Report No. CMS-PAS-EXO-19-018, 2020, https://cds.cern.ch/record/2684861.
[40] M. Karliner, M. Low, J. L. Rosner, and L.-T. Wang, Radiative return capabilities of a high-energy, high-luminosity e^+e^- collider, Phys. Rev. D **92**, 035010 (2015).
[41] S. Snyder, C. Weber, and D. Zhang, Prospects for searches for Higgs boson decays to dark photons at the ILC, in *Snowmass 2021* (2022), 3, arXiv:2203.08270.
[42] C. M. Berggren and S. Hosseini-Servan (ILD Concept Group Collaboration), Search for dark photons at future e^+e^- colliders, Proc. Sci. EPS-HEP2023 (**2024**) 047.
[43] M. He, X.-G. He, and C.-K. Huang, Dark photon search at a circular e^+e^- collider, Int. J. Mod. Phys. A **32**, 1750138 (2017).
[44] C. Cesarotti and G. Krnjaic, Hitting the thermal target for leptophilic dark matter, arXiv:2404.02906.
[45] D. Curtin, R. Essig, S. Gori, and J. Shelton, Illuminating dark photons with high-energy colliders, J. High Energy Phys. 02 (2015) 157.
[46] N. Arkani-Hamed, T. Han, M. Mangano, and L. T. Wang, Physics opportunities of a 100 TeV proton–proton collider, Phys. Rep. **652**, 1 (2016).
[47] R. Palmer *et al.*, Muon collider design, Nucl. Phys. B, Proc. Suppl. **51**, 61 (1996).
[48] C. M. Ankenbrandt *et al.*, Status of muon collider research and development and future plans, Phys. Rev. ST Accel. Beams **2**, 081001 (1999).
[49] D. Schulte (Muon Collider Collaboration), The International Muon Collider Collaboration, JACoW **IPAC2021**, 3792 (2021).
[50] R. Capdevilla, D. Curtin, Y. Kahn, and G. Krnjaic, Discovering the physics of $(g-2)_\mu$ at future muon colliders, Phys. Rev. D **103**, 075028 (2021).
[51] P. Bandyopadhyay, A. Karan, R. Mandal, and S. Parashar, Distinguishing signatures of scalar leptoquarks at hadron and muon colliders, Eur. Phys. J. C **82**, 916 (2022).
[52] C. Sen, P. Bandyopadhyay, S. Dutta, and A. KT, Displaced Higgs production in Type-III seesaw at the LHC/FCC, MATHUSLA and muon collider, Eur. Phys. J. C **82**, 230 (2022).
[53] P. Asadi, R. Capdevilla, C. Cesarotti, and S. Homiller, Searching for leptoquarks at future muon colliders, J. High Energy Phys. 10 (2021) 182.
[54] G.-y. Huang, F. S. Queiroz, and W. Rodejohann, Gauged $L_\mu - L_\tau$ at a muon collider, Phys. Rev. D **103**, 095005 (2021).
[55] C. Accettura *et al.*, Towards a muon collider, Eur. Phys. J. C **83**, 864 (2023); **84**, 36(E) (2024).
[56] H. Al Ali *et al.*, The muon Smasher's guide, Rep. Prog. Phys. **85**, 084201 (2022).
[57] A. Azatov, F. Garosi, A. Greljo, D. Marzocca, J. Salko, and S. Trifinopoulos, New physics in $b \to s\mu\mu$: FCC-hh or a muon collider?, J. High Energy Phys. 10 (2022) 149.
[58] K. Mekala, J. Reuter, and A. F. Zarnecki, Discriminating Majorana and Dirac heavy neutrinos at lepton colliders, J. High Energy Phys. 03 (2024) 075.
[59] M. Palmer, Muon Collider Design, in *Community Summer Study on the Future of U.S. Particle Physics (Snowmass on the Mississippi), Minneapolis, MN, USA* (American Physical Society, Minneapolis, 2013).
[60] M. Antonelli, M. Boscolo, R. Di Nardo, and P. Raimondi, Novel proposal for a low emittance muon beam using

positron beam on target, Nucl. Instrum. Methods Phys. Res., Sect. A **807**, 101 (2016).
[61] F. Collamati, C. Curatolo, D. Lucchesi, A. Mereghetti, N. Mokhov, M. Palmer, and P. Sala, Advanced assessment of beam-induced background at a muon collider, J. Instrum. **16**, P11009 (2021).
[62] D. Ally, L. Carpenter, T. Holmes, L. Lee, and P. Wagenknecht, Strategies for beam-induced background reduction at muon colliders, in Snowmass 2021 (2022), 3, arXiv:2203.06773.
[63] Y. Hosseini and M. M. Najafabadi, Unitarity constraints and collider searches for dark photons, Phys. Rev. D **106**, 015028 (2022).
[64] N. Chakrabarty, T. Han, Z. Liu, and B. Mukhopadhyaya, Radiative return for heavy Higgs boson at a muon collider, Phys. Rev. D **91**, 015008 (2015).
[65] P. Draper, J. Kozaczuk, and S. Thomas, Precision inclusive Higgs physics at e^+e^- colliders with tracking detectors and without calorimetry, J. High Energy Phys. 09 (2020) 174,
[66] T. Han, D. Liu, I. Low, and X. Wang, Electroweak couplings of the Higgs boson at a multi-TeV muon collider, Phys. Rev. D **103**, 013002 (2021).
[67] Y. Zhu, H. Cui, and M. Ruan, The Higgs $\to b\bar{b}, c\bar{c}$, gg measurement at CEPC, J. High Energy Phys. 11 (2022) 100.
[68] Q. ShaQ. Sha, A. Fadol, F. Guo, Y. Fang, J. Gu, and X. Lou, Probing Higgs *CP* properties at the CEPC in the $e^+e^- \to ZH \to l^+l^-H$ using optimal variables, Eur. Phys. J. C **82**, 981 (2022); **83**, 62(E) (2023).
[69] A. Dasgupta, P. S. B. Dev, T. Han, R. Padhan, S. Wang, and K. Xie, Searching for heavy leptophilic Z': From lepton colliders to gravitational waves, J. High Energy Phys. 12 (2023) 011.
[70] M. Chen and D. Liu, Top Yukawa coupling measurement at the muon collider, Phys. Rev. D **109**, 075020 (2024).
[71] H. Denizli, A. Senol, and M. Köksal, Probing the electromagnetic properties of the neutrinos at future lepton colliders, Phys. Lett. B **853**, 138648 (2024).
[72] M. Forslund and P. Meade, Precision Higgs width and couplings with a high energy muon collider, J. High Energy Phys. 01 (2024) 182.
[73] R. Jiang, C. Jiang, A. Ruzi, T. Yang, Y. Ban, and Q. Li, Searches for multi-Z boson productions and anomalous gauge boson couplings at a muon collider*, Chin. Phys. C **48**, 103102 (2024).
[74] P. Li, Z. Liu, and K.-F. Lyu, Higgs boson width and couplings at high energy muon colliders with forward muon detection, Phys. Rev. D **109**, 073009 (2024).
[75] A. K. Barik, S. K. Rai, and A. Srivastava, Discovering an invisible Z' at the muon collider, Phys. Lett. B **866**, 139533 (2025).
[76] G. Abbiendi *et al.* (OPAL Collaboration), Two Higgs doublet model and model independent interpretation of neutral Higgs boson searches, Eur. Phys. J. C **18**, 425 (2001).
[77] Q.-H. Cao, K. Cheng, and Y. Liu, Distinguishing Dirac from Majorana heavy neutrino at future lepton colliders, Phys. Rev. Lett. **134**, 021801 (2025).
[78] H. Hyun (Belle Collaboration), Search for an exotic light particle at Belle, in *25th Lake Louise Winter Institute: Celebrating 25 Years* (2010), 6, arXiv:1006.1037.
[79] A. Filippi (*BABAR* Collaboration), Dark photon studies at *BABAR*, EPJ Web Conf. **218**, 06001 (2019).
[80] I. Adachi *et al.* (Belle-II Collaboration), Search for an invisibly decaying Z' boson at Belle II in $e^+e^- \to \mu^+\mu^-(e^\pm\mu^\mp)$ plus missing energy final states, Phys. Rev. Lett. **124**, 141801 (2020).
[81] Y. Wang, M. Berggren, and J. List, ILD Benchmark: Search for extra scalars produced in association with a Z boson at $\sqrt{s} = 500$ GeV, arXiv:2005.06265.
[82] Y. C. San, M. Perelstein, and P. Tanedo, Dark Z at the International Linear Collider, Phys. Rev. D **106**, 015027 (2022).
[83] K. Cheung, W. Hsiao, C. J. Ouseph, and C. Wang, Probing the gauge-boson couplings of axion-like particle at the LHC and high-luminosity LHC, J. High Energy Phys. 05 (2024) 324.
[84] J. de Favereau, C. Delaere, P. Demin, A. Giammanco, V. Lemaître, A. Mertens, and M. Selvaggi (DELPHES 3 Collaboration), DELPHES 3, A modular framework for fast simulation of a generic collider experiment, J. High Energy Phys. 02 (2014) 057.
[85] H. Ruegg and M. Ruiz-Altaba, The Stueckelberg field, Int. J. Mod. Phys. A **19**, 3265 (2004).
[86] W. Abdallah, A. K. Barik, S. K. Rai, and T. Samui, Search for a light Z' at LHC in a neutrinophilic U(1) model, Phys. Rev. D **104**, 095031 (2021).
[87] S. Schael *et al.* (ALEPH, DELPHI, L3, OPAL, LEP Electroweak Collaborations), Electroweak measurements in electron-positron collisions at W-boson-pair energies at LEP, Phys. Rep. **532**, 119 (2013).
[88] G. Aad *et al.* (ATLAS Collaboration), Search for high-mass dilepton resonances using 139 fb^{-1} of pp collision data collected at $\sqrt{s} = 13$ TeV with the ATLAS detector, Phys. Lett. B **796**, 68 (2019).
[89] M. Aaboud *et al.* (ATLAS Collaboration), Search for additional heavy neutral Higgs and gauge bosons in the ditau final state produced in 36 fb^{-1} of pp collisions at $\sqrt{s} = 13$ TeV with the ATLAS detector, J. High Energy Phys. 01 (2018) 055.
[90] M. Aaboud *et al.* (ATLAS Collaboration), Search for lepton-flavor violation in different-flavor, high-mass final states in pp collisions at $\sqrt{s} = 13$ TeV with the ATLAS detector, Phys. Rev. D **98**, 092008 (2018).
[91] A. M. Sirunyan *et al.* (CMS Collaboration), Search for lepton-flavor violating decays of heavy resonances and quantum black holes to eμ final states in proton-proton collisions at $\sqrt{s} = 13$ TeV, J. High Energy Phys. 04 (2018) 073.
[92] M. Aaboud *et al.* (ATLAS Collaboration), Search for heavy resonances decaying to a W or Z boson and a Higgs boson in the $q\bar{q}^{(\prime)}b\bar{b}$ final state in pp collisions at $\sqrt{s} = 13$ TeV with the ATLAS detector, Phys. Lett. B **774**, 494 (2017).
[93] A. M. Sirunyan *et al.* (CMS Collaboration), Search for a heavy vector resonance decaying to a Z boson and a Higgs

boson in proton-proton collisions at $\sqrt{s} = 13$TeV, Eur. Phys. J. C **81**, 688 (2021).
[94] A. M. Sirunyan *et al.* (CMS Collaboration), Search for an $L_\mu - L_\tau$ gauge boson using $Z \to 4\mu$ events in proton-proton collisions at $\sqrt{s} = 13$ TeV, Phys. Lett. B **792**, 345 (2019).
[95] M. Aaboud *et al.* (ATLAS Collaboration), Search for Higgs boson decays to beyond-the-standard-model light bosons in four-lepton events with the ATLAS detector at $\sqrt{s} = 13$ TeV, J. High Energy Phys. 06 (2018) 166.
[96] G. Aad *et al.* (ATLAS Collaboration), Search for diboson resonances in hadronic final states in 139 fb^{-1} of pp collisions at $\sqrt{s} = 13$ TeV with the ATLAS detector, J. High Energy Phys. 09 (2019) 091; 06 (2020) 042(E).
[97] A. M. Sirunyan *et al.* (CMS Collaboration), A multi-dimensional search for new heavy resonances decaying to boosted WW, WZ, or ZZ boson pairs in the dijet final state at 13 TeV, Eur. Phys. J. C **80**, 237 (2020).
[98] V. M. Abazov *et al.* (D0 Collaboration), Search for a heavy neutral gauge boson in the dielectron channel with 5.4 fb^{-1} of $p\bar{p}$ collisions at $\sqrt{s} = 1.96$ TeV, Phys. Lett. B **695**, 88 (2011).
[99] M. Casarsa, D. Lucchesi, and L. Sestini, Experimentation at a muon collider, Annu. Rev. Nucl. Part. Sci. **74**, 233 (2024).
[100] N. Bartosik, A. Bertolin, M. Casarsa, F. Collamati, A. Ferrari, A. Ferrari, A. Gianelle, D. Lucchesi, N. Mokhov, S. Mueller *et al.*. Preliminary report on the study of beam-induced background effects at a muon collider, arXiv:1905.03725.
[101] J. Alwall, M. Herquet, F. Maltoni, O. Mattelaer, and T. Stelzer, MadGraph5: Going beyond, J. High Energy Phys. 06 (2011) 128.
[102] A. Costantini, F. De Lillo, F. Maltoni, L. Mantani, O. Mattelaer, R. Ruiz, and X. Zhao*et al.*, Vector boson fusion at multi-TeV muon colliders, J. High Energy Phys. 09 (2020) 080.
[103] C. Accettura *et al.* (International Muon Collider Collaboration), The muon collider, arXiv:2504.21417.
[104] M. Chiesa, F. Maltoni, L. Mantani, B. Mele, F. Piccinini, and X. Zhao, Measuring the quartic Higgs self-coupling at a multi-TeV muon collider, J. High Energy Phys. 09 (2020) 098,
[105] K. M. Black *et al.*, Muon collider forum report, J. Instrum. **19**, T02015 (2024).
[106] M. H. Wang, Y. Nosochkov, Y. Cai, and M. Palmer, Design of a 6 TeV muon colliderJ. Instrum. **11**, P09003 (2016).
[107] T. Han, Z. Liu, L. T. Wang, and X. Wang, WIMP dark matter at high energy muon colliders -a white paper for snowmass 2021arXiv:2203.07351.
[108] W. Altmannshofer, S. A. Gadam, and S. Profumo, Probing new physics with $\mu + \mu$- $\to$ bs at a muon collider, Phys. Rev. D **108** (2023) 115033.
[109] P. Bandyopadhyay, S. Parashar, C. Sen, and J. Song, Probing Inert Triplet Model at a multi-TeV muon collider via vector boson fusion with forward muon tagging, J. High Energy Phys. 07 (2024) 253.
[110] J. de Blas *et al.* (Muon Collider Collaboration), The physics case of a 3 TeV muon collider stage, arXiv: 2203.07261.
[111] C. Accettura *et al.* (MuCoL Collaboration), MuCol Milestone Report No. 5: Preliminary Parameters, 10.5281/zenodo.13970100.
[112] C. Bell *et al.* (MAIA Collaboration, MAIA: A new detector concept for a 10 TeV muon collider, arXiv:2502.00181.
[113] C. Bierlich *et al.*, A comprehensive guide to the physics and usage of PYTHIA 8.3, SciPost Phys. Codebases **2022**, 8 (2022).
[114] J. P. Delahaye, M. Diemoz, K. Long, B. Mansoulié, N. Pastrone, L. Rivkin *et al.*, Muon colliders, arXiv:1901.06150.
[115] K. Long, D. Lucchesi, M. Palmer, N. Pastrone, D. Schulte, and V. Shiltsev, Muon colliders to expand frontiers of particle physics, Nat. Phys. **17**, 289 (2021).
[116] M. Ruhdorfer, E. Salvioni, and A. Wulzer, Invisible Higgs boson decay from forward muons at a muon collider, Phys. Rev. D **107**, 095038 (2023).
[117] M. Boronat, J. Fuster, I. Garcia, E. Ros, and M. Vos, A robust jet reconstruction algorithm for high-energy lepton colliders, Phys. Lett. B **750**, 95 (2015).
[118] M. Boronat, J. Fuster, I. Garcia, P. Roloff, R. Simoniello, and M. Vos, Jet reconstruction at high-energy electron–positron colliders, Eur. Phys. J. C **78**, 144 (2018).
[119] M. Cacciari, G. P. Salam, and G. Soyez, FastJet user manual, Eur. Phys. J. C **72**, 1896 (2012).
[120] M. Dasgupta, K. Khelifa-Kerfa, S. Marzani, and M. Spannowsky, On jet mass distributions in Z + jet and dijet processes at the LHC, J. High Energy Phys. 10 (2012) 126.
[121] G. Cowan, K. Cranmer, E. Gross, and O. Vitells, Asymptotic formulae for likelihood-based tests of new physics, Eur. Phys. J. C **71**, 1554 (2011); **73**, 2501(E) (2013).
[122] A. Abada *et al.* (FCC Collaboration), FCC-hh: The hadron collider: Future circular collider conceptual design report volume 3, Eur. Phys. J. Special Topics **228**, 755 (2019).